



## An expanded workflow for detrital rutile provenance studies: An application from the Neotethys Orogen in Anatolia

Megan A. Mueller<sup>1,2,\*</sup>, Alexis Licht<sup>2,3</sup>, Andreas Möller<sup>4</sup>, Cailey B. Condit<sup>2</sup>, Julie C. Fosdick<sup>1</sup>, Faruk Ocakoğlu<sup>5</sup>, Clay Campbell<sup>6</sup>

5 <sup>1</sup> Department of Earth Sciences, University of Connecticut, 354 Mansfield Road - Unit 1045, Storrs, CT 06269

<sup>2</sup> Department of Earth and Space Sciences, University of Washington, 4000 15th Avenue NE, Seattle, WA 98195

<sup>3</sup> Aix-Marseille Université, CNRS, IRD, INRAE, Collège de France, CEREGE, Technopôle de l'Arbois-Méditerranée, BP80, 13545 Aix-en-Provence, France

<sup>4</sup> Department of Geology, The University of Kansas, 1414 Naismith Drive, Lawrence, KS 66045

10 <sup>5</sup> Department of Geological Engineering, Eskişehir Osmangazi University, Büyükdere, 26040 Eskişehir, Türkiye

<sup>6</sup> Department of Geosciences, University of Arizona, 1040 E 4th St, Tucson, AZ 85721

\* Now at Department of Geological Sciences, Jackson School of Geosciences, The University of Texas at Austin, 2305 Speedway Stop C1160, Austin, TX 78712

*Correspondence to:* Megan Mueller (megan.mueller@jsg.utexas.edu)

15 **Abstract.** Sedimentary provenance is a powerful tool for reconstructing convergent margin evolution. Yet single mineral approaches, like detrital zircon, have struggled to track sediment input from mafic and metamorphic sources. Sediment input from these lithologies is especially critical for reconstructing orogenic settings dominated by terrane accretion, ophiolite obduction, and forearc inversion. Rutile can form in metamorphic and igneous rocks and hydrothermal veins, and its U-Pb age and geochemistry often records cooling from the most recent medium to high grade metamorphic event. Thus, detrital rutile complements detrital zircon datasets by offering a path forward in sedimentary provenance reconstructions when metamorphic terranes are potential source regions. However, U-Pb geochronology in rutile can be difficult due to low uranium concentrations and high discordance. **Here, we present detrital rutile U-Pb geochronology and trace element geochemistry results from the Late Cretaceous to Eocene Central Sakarya and Sarıcakaya Basins in Anatolia to reconstruct provenance during Neotethys orogenesis.** The resulting detrital rutile U-Pb analyses are highly discordant due to the incorporation of non-radiogenic initial Pb. We present a new workflow that accounts for low-U rutile and is based on common Pb corrections and discordance filters. The resulting age spectra are similar for grains up to 40% concordant (60% discordant) and across the common Pb correction methods, thus providing a path forward to confidently interpret provenance from discordant rutile grains. Together, the detrital rutile trace element geochemistry and Zr-in-rutile thermometry indicate sediment was sourced from mixed metamafic and metapelitic units with low-grade metamorphic temperatures. Low-U concentration rutile are numerous and more discordant and were predominantly sourced from Late Triassic-Early Jurassic greenschist and blueschist facies rocks with both mafic and pelitic lithologies. This corresponds to sediment derived from the Karakaya Complex, a Paleozoic subduction-accretion complex or oceanic plateau that was accreted and metamorphosed in the Triassic-Jurassic, exhumed to the surface in the Jurassic, and then deformed during Neotethys suturing in the Late Cretaceous to Paleogene. Late Triassic-Early Jurassic ages are nearly absent from the detrital zircon record, emphasizing that a multi-mineral approach, especially inclusive of low-U rutile, provides a more holistic provenance



reconstruction. These detrital rutile results serve as an additional layer of data often unexplored across convergent margins globally, and thus provide an exciting path forward in characterizing diverse provenance of orogenic settings.

## 1 Introduction

40 The acceptance of plate tectonics brought about the recognition that sediment deposited in convergent margin basins archives orogenesis (Hubert, 1971; Dickinson, 1974; Morton, 1985). Sedimentary provenance analysis is widely used to reconstruct ancient sediment dispersal networks, source-to-sink sediment budgets, sedimentary basin evolution, and to discern links between tectonics, geodynamics, paleogeography, climate, and biologic evolution (Dickinson and Suczek, 1979; Garzanti et al., 2007; Clift et al., 2008; Gehrels, 2014; Blum and Pecha, 2014). Not  
45 only do sedimentary basins archive these processes in their stratigraphic architecture and environments of deposition, but they are often the best, and sometimes only, record of these processes in deep time. In convergent margin settings, sedimentary provenance analysis uses the mineralogical and geochemical composition of sedimentary rocks to interpret changes in sediment source as a function of geodynamics, deformation, topography, climate, and paleogeography (e.g., Morton and Hallsworth, 1994; Garzanti, 2018).

50 Classic provenance methods include bulk sediment petrologic, chemical, and heavy mineral characterizations (e.g., Gazzi, 1965; Hubert, 1971; Dickinson and Suczek, 1979; Morton, 1985; Garzanti and Andò, 2007). Over the last several decades, the rise of chronometric and geochemical techniques has elevated single-mineral approaches. Detrital zircon U-Pb geochronology has become the gold standard technique (e.g., Gehrels, 2014): the age, thermal history, and elemental and isotopic composition of detrital zircons can quantitatively reconstruct both sedimentary  
55 provenance and geodynamic, tectonic, and magmatic processes (Carrapa, 2010; Paterson and Ducea, 2015; Tang et al., 2020; Sundell et al., 2022). However, one major limitation is that zircons predominantly form in intermediate to felsic magmas, thus detrital zircon suites generally lack information about mafic igneous and metamorphic processes and sources (Hietpas et al., 2011; Moecher et al., 2011; Gaschnig, 2019). Although zircon is present in metamorphic rocks as small inclusions in other minerals or as recrystallized-dissolved-reprecipitated rims on zircon cores (Kohn and Kelly, 2017), the standard detrital zircon U-Pb geochronology techniques for rapid provenance data acquisition  
60 (i.e., laser ablation ICP-MS) do not routinely analyze zircon rims. Therefore, sedimentary provenance interpretations based on detrital zircon alone are incomplete. For this reason the sedimentary provenance community is increasingly turning to phases commonly used in petrochronology, such as detrital rutile (Zack et al., 2004a; Meinhold, 2010; Triebold et al., 2012; Bracciali et al., 2013; Rösel et al., 2014, 2019; Pereira et al., 2020), detrital monazite (Hietpas et al., 2010; Moecher et al., 2011; Gaschnig, 2019), and detrital titanite (Guo et al., 2020; Chew et al., 2020). The  
65 ‘zircon problem’ is especially pronounced in continental collision and accretionary orogenic settings where obducted ophiolites, ophiolitic mélangé, metamafic and metapelitic terranes, and exhumed metamorphic massifs are commonly exposed, and the P-T-t history of these units pinpoint important geodynamic milestones.

Detrital rutile is a promising sedimentary provenance proxy to overcome this zircon problem. Rutile can form  
70 in metamafic and metapelitic rocks across a range of P-T conditions, therefore, detrital rutile is especially advantageous when tracking sediment input from greenschist to eclogite facies sources (e.g., Zack and Kooijman, 2017). With a U-Pb closure temperature of 490–640°C (Kooijman et al., 2010), while U-Pb dates correspond cooling



75 **from the most recent medium to high-temperature metamorphic event that exceeded the closure temperature** (Zack et al., 2004b; Zack and Kooijman, 2017). Hence, first-cycle detrital rutile can track sediment input **from metamorphic** units. The geochemical composition (Cr/Nb) can further distinguish between metamorphic protoliths (e.g., Triebold et al., 2007, 2012; Meinhold, 2010). **Analytically, though, U-Pb geochronology** in rutile can be difficult due to low uranium concentrations. For this reason, some studies only analyze or interpret detrital rutile above a given U threshold (ca. > 4-5 ppm; e.g., Zack et al., 2004a; Okay et al., 2011; Rösel et al., 2019). However, this analytical approach likely biases provenance results as the concentration of uranium in rutile systematically varies by metamorphic protoliths, with mafic eclogites having lower U contents than metapelites (e.g., Meinhold, 2010).

80 Here, we investigate the limitations of U-threshold filtering with a new dataset from Anatolia inclusive of all rutile, where low-U rutile grains are numerous and diagnostic of specific metamorphic units. We build a new workflow that includes low-U rutile and tests different common Pb correction approaches. Furthermore, we test the sensitivity of resulting U-Pb age spectra to the Pb correction methods and to discordance filters and determine whether these factors alter the overall provenance interpretation. Overall, this new dataset demonstrates that detrital rutile captures sediment input from a subduction accretion complex that is poorly resolved in the detrital zircon record.

## 2 Detrital Rutile Provenance

### 2.1 Detrital Rutile Synopsis

90 The utility of detrital rutile is extensively documented (e.g., Zack et al., 2004a; Meinhold, 2010; Triebold et al., 2012; Gaschnig, 2019; ~~Ma~~ **Ma** et al., 2020; Pereira and Storey, 2023), so here we provide only a brief overview. Rutile is the most common TiO<sub>2</sub> polymorph, a common accessory mineral in metamorphic and igneous rocks (**Zack and Kooijman, 2017**), and an abundant heavy mineral in sedimentary rocks (Morton, 1985). ~~During prograde metamorphism, rutile crystallizes from ilmenite and biotite (Luvizotto et al., 2009; Meinhold, 2010) and rutile's chemical composition preserves original petrogenetic information.~~ Rutile concentrates high field strength elements (Zr, Nb, Mo, Sn, Sb, Hf, Ta, W) through substitution with Ti that are commonly used as fingerprints of subduction zone metamorphism and crustal evolution (e.g., Nb and Ta; Rudnick et al., 2000). Detrital rutile geochemistry fingerprints sediment sources in **several** unique ways. First, rutile concentrates the vast majority of available Nb whereas Cr is non-selective and is distributed across metamorphic minerals; therefore the Cr and Nb concentrations in rutile can discriminate between metamafic and metapelitic lithologies (Zack et al., 2004a, b; Triebold et al., 2011, 2012). ~~Cr and Nb concentrations are attributed to different protoliths: metapelitic rutile (i.e. mica schists, paragneisses, felsic granulites) have Cr < Nb and metabasic rutile (i.e., mafic eclogites and granulites) have Cr > Nb, generally (Zack et al., 2004b).~~ Second, the incorporation of Zr in rutile is largely temperature dependent (Zack et al., 2004b; Watson et al., 2006; Tomkins et al., 2007; Ferry and Watson, 2007). Zirconium mobilizes during prograde metamorphic fluid release; the incorporation of Zr into rutile is buffered by coexisting quartz and zircon (Zack et al., 2004b). Zr contents in rutile correlate with peak metamorphic temperature and pressure conditions (Zack et al., 2004b; Watson et al., 2006; Tomkins et al., 2007; Kohn, 2020). Therefore, the Zr elemental composition in rutile is a commonly used thermometer, empirically and experimentally calibrated across a range of pressures and



thermodynamic activity parameters (Zack et al., 2004b; Watson et al., 2006; Tomkins et al., 2007; Kohn, 2020). In detrital minerals, which are removed from the context of constitutive relationships (i.e., pressure and silica activity), these thermometers can provide an estimate of the minimum peak metamorphic temperatures (Rösel et al., 2019). For rutile of unknown source lithology, the calculated temperature is affected by the chosen pressure; Pereira and Storey (2023) demonstrate this pressure dependence in detrital grains, and therefore recommend using the experimental and empirical calibration of Kohn (2020; their eqn. 13) at an average pressure of 13 kbar with an uncertainty of 5 kbar:

$$T \text{ (}^\circ\text{C)} = \frac{71360 + 0.378 \cdot P(\text{bars}) - 0.130 \cdot C(\text{ppm})}{130.66 - R \cdot \ln[C(\text{ppm})]} - 273.15 \quad (1)$$

where C is the concentration of Zr in ppm and R is the gas constant, 8.3144.

## 2.2 Detrital Rutile Challenge #1: Low Uranium Contents

Detrital rutile U-Pb petrochronology presents unique analytical, data reduction, and interpretation challenges. Uranium concentration in rutile varies among metamorphic protoliths: for example, rutile from mafic eclogites have, on average, 75% less U than those from metapelites (i.e., 5 ppm vs. 21 ppm; Meinhold, 2010). Analytically, the low U concentrations in rutile, predominantly sourced from mafic lithologies, can make it challenging to date. To optimize data collection, many detrital rutile methods first analyze trace elements then only collect U-Pb data on rutile above a given U concentration threshold (ca. > 4–5 ppm; e.g., Zack et al., 2004a; Okay et al., 2011; Rösel et al., 2019). As expected, screening low-U rutile produces a higher proportion of concordant analyses and reduces the overall length of U-Pb analytical sessions, but introduces bias into the provenance results against metamafic rocks. Screening low-U rutile may make sense in some geologic settings based on the lithology of potential sediment sources; however, metamafic units in suture zones, presumably with low-U rutile, are expected to be a major contributor of detritus to many orogenic basins, including the northwestern Anatolian basins of this study. Therefore, we explore whether analyzing detrital rutile of all U concentrations offers the opportunity to reconstruct a completer and more representative sedimentary provenance in forearc and suture zone settings during subduction and collision.

## 2.3 Detrital Rutile Challenge #2: Common Pb Incorporation

A second challenge with detrital rutile lies with data reduction and presentation. The U-Pb system in rutile is different from that of zircon, for example, due to the incorporation of common Pb, thereby requiring careful methodological choices on how to treat non-radiogenic Pb and U-Pb discordance. The zircon U-Pb system is ‘simple’ in the sense that zircon incorporates negligible non-radiogenic initial or ‘common’ Pb during crystallization, and Pb diffuses only at extremely high temperatures and in zircon with radiation damage (e.g., Schoene, 2014 and references therein). Thus, the majority of detrital zircon U-Pb analyses tend to be close to concordia, and significant discordance is dominantly controlled by recent Pb loss facilitated by radiation damage accumulation (Nasdala et al., 1998). This makes data reduction and interpretation more straightforward, as even the  $^{207}\text{Pb}/^{206}\text{Pb}$  dates of moderately discordant zircon are likely to be meaningful. Rutile, on the other hand, can incorporate significant common Pb, can have low U contents, and is more sensitive to thermally activated Pb diffusion over a wide range of lithospheric thermal conditions.



Therefore, most rutile U-Pb dates are expected to be discordant. *In-situ* studies mitigate this by: (1) regressing discordia lines through co-genetic analyses in Tera-Wasserburg space, where the lower intercept of the discordia with the concordia defines the U-Pb age of Pb diffusion closure (Faure, 1986; Chew et al., 2011; Vermeesch, 2020); or (2) applying a non-radiogenic Pb correction using either an *ad hoc* Pb model such as that of Stacey and Kramers (1975), or measuring the composition of non-radiogenic Pb in a co-existing phase. However, by nature, the co-genetic grains in detrital samples are unknown. This creates a first-order methodological hurdle for detrital petrochronology: *what is the best way to determine the U-Pb age for discordant detrital analyses?*; and *do different discordance filters influence the resulting age spectra and provenance interpretations or not?* This careful methodological step is critical to produce age distributions that can be interpreted confidently. Below we review <sup>208</sup>Pb-based and <sup>207</sup>Pb-based methods for calculating U-Pb dates in discordant grains, then we illustrate this comparison with a new dataset from Anatolia.

### 2.3.1 <sup>208</sup>Pb Correction

The <sup>208</sup>Pb correction method determines the common Pb component using the <sup>232</sup>Th-<sup>208</sup>Pb decay scheme and assumes U-Th-Pb concordance and no Pb loss. The <sup>208</sup>Pb correction is ideal for low-Th phases (Zack et al., 2011) and is commonly used for rutile, although not all rutile have low Th concentrations. This method here directly follows the method of Chew et al. (2011) and Odlum et al. (2019), which is also discussed in McLean et al. (2011) and as the total-Pb/U-Th scheme in Vermeesch (2020).

The proportion of <sup>206</sup>Pb<sub>common</sub> is calculated as

$$f_{206} = \frac{(^{208}\text{Pb}/^{206}\text{Pb})_{\text{measured}} - (^{208}\text{Pb}^*/^{206}\text{Pb}^*)}{(^{208}\text{Pb}/^{206}\text{Pb})_{\text{common}} - (^{208}\text{Pb}^*/^{206}\text{Pb}^*)} \quad (2)$$

where <sup>208</sup>Pb/<sup>206</sup>Pb<sub>measured</sub> is calculated directly from the raw data. The <sup>208</sup>Pb/<sup>206</sup>Pb<sub>common</sub> ratio is calculated from the two-stage Pb evolution model of Stacey and Kramers (1975) for dates younger than 3.7 Ga using t<sub>i</sub>:

$$\left(\frac{^{206}\text{Pb}}{^{204}\text{Pb}}\right)_{\text{common}} = 9.74 \cdot (e^{\lambda_{238} \cdot 3.7 \times 10^9} - e^{\lambda_{238} \cdot t_i}) + 11.152 \quad (3)$$

and

$$\left(\frac{^{208}\text{Pb}}{^{204}\text{Pb}}\right)_{\text{common}} = 36.84 \cdot (e^{\lambda_{232} \cdot 3.7 \times 10^9} - e^{\lambda_{232} \cdot t_i}) + 31.23 \quad (4)$$

and the expected radiogenic <sup>208</sup>Pb\*/<sup>206</sup>Pb\* ratios are calculated as

$$\frac{^{208}\text{Pb}^*}{^{206}\text{Pb}^*} = \left(\frac{^{232}\text{Th}}{^{238}\text{U}}\right) \cdot \left(\frac{e^{\lambda_{232} t_i} - 1}{e^{\lambda_{238} t_i} - 1}\right) \quad (5)$$

where t<sub>i</sub> is the uncorrected date in years. Then, the radiogenic component, the <sup>206</sup>Pb\*/<sup>238</sup>U ratio, can be calculated as



$${}^{206}\text{Pb}^*/{}^{238}\text{U} = (1 - f_{206}) \cdot ({}^{206}\text{Pb}/{}^{238}\text{U}_{\text{measured}}). \quad (6)$$

The  ${}^{208}\text{Pb}$ -corrected date ( ${}^{206}\text{Pb}^*/{}^{238}\text{U}$  date) is calculated by solving the age equation with the  ${}^{206}\text{Pb}^*/{}^{238}\text{U}$  ratio. To iteratively calculate the date, each iteration replaces  $t_i$  with the previously calculated  ${}^{206}\text{Pb}^*/{}^{238}\text{U}$  date. The  ${}^{208}\text{Pb}$ -corrected date presented here is from the fifth iteration. The error on the date is calculated as the equivalent of the percent error of the uncorrected  ${}^{206}\text{Pb}/{}^{238}\text{U}$  date (Odlum et al., 2019).

### 2.3.2 ${}^{207}\text{Pb}$ Correction

The  ${}^{207}\text{Pb}$  correction method is based on a linear regression of  ${}^{207}\text{Pb}/{}^{206}\text{Pb}$  and  ${}^{238}\text{U}/{}^{206}\text{Pb}$  in Tera-Wasserburg space (Tera and Wasserburg, 1972) along a two-component mixing line between non-radiogenic and radiogenic Pb (Faure, 1986). This method is most powerful for cogenetic minerals because it does not require knowing  ${}^{207}\text{Pb}/{}^{206}\text{Pb}_{\text{common}}$ . Yet, because cogenetic analyses are inherently unknown in detrital samples, the routine used here calculates the common Pb component of each individual analysis using the Stacey and Kramers (1975) two-stage Pb evolution model and an initial age estimate. We explore using an initial date estimate from the uncorrected date ( $t_i$ ) and from the  ${}^{208}\text{Pb}$ -corrected date ( $t_{208}$ ). The intersection of the discordia with the concordia curve, anchored by  ${}^{207}\text{Pb}/{}^{206}\text{Pb}_{\text{common}}$ , is the radiogenic  ${}^{207}\text{Pb}/{}^{206}\text{Pb}^*$ . To find the intersection, we use the Schwarz (2022) intersection function in MATLAB. The  ${}^{207}\text{Pb}$ -corrected  ${}^{207}\text{Pb}/{}^{206}\text{Pb}^*$  and  ${}^{206}\text{Pb}^*/{}^{238}\text{U}$  dates are calculated from  ${}^{207}\text{Pb}/{}^{206}\text{Pb}^*$  and  ${}^{206}\text{Pb}^*/{}^{238}\text{U}$ , respectively. Note that because the correction forces intersection with the concordia, the two dates are identical. Discordance is calculated in Tera-Wasserburg space, where the percent discordance is defined as the distance between the measured  ${}^{238}\text{U}/{}^{206}\text{Pb}$  and  ${}^{207}\text{Pb}/{}^{206}\text{Pb}$  coordinates and the concordia intersection ( $\delta_2$ ) along the total discordia line distance ( $\delta_1 + \delta_2$ ) (Figure 1, Vermeesch, 2021):

$$\text{Concordance} = \delta_1 / (\delta_1 + \delta_2) \quad (7)$$

This version of discordance, when applied with a stricter filter, is more forgiving, dates younger than 1000 Ma where the slope of the concordia curve is shallow (Vermeesch, 2021).

Like the  ${}^{208}\text{Pb}$  correction method, the  ${}^{207}\text{Pb}$  correction method assumes U-Pb concordance and no Pb loss. Because Pb loss is not considered, all calculated dates are obtained from lower intercepts are (possibly) minimum ages. The method here is modified for detrital samples with unknown cogenetic minerals based on methods in Faure (1986), Chew et al. (2011), and the semitotal-Pb/U scheme of Ludwig (1998) and Vermeesch (2020).

We illustrate the difference between these different Pb correction methods and the issue raised by low-U screening with a new dataset from Anatolia.

## 3. Geologic Context

Anatolia is composed of a series of subduction complexes, island arcs, and continental terranes that accreted and collided from the Late Paleozoic through Cenozoic during the progressive opening and closing of Paleotethys and Neotethys seaways (Şengör and Yilmaz, 1981). Today, northwestern Anatolia comprises, from north to south, the



continental Pontides, including the Cretaceous–Eocene forearc-to-foreland Central Sakarya and Sarıcakaya Basins, the Permian–Triassic Karakaya Complex, the İzmir–Ankara–Erzincan suture zone and associated Neotethys ophiolites and mélange, and the lower plate Anatolide–Tauride continental terranes (Figure 2). The Pontides basement contains Paleozoic paragneiss, schist, and amphibolite rocks intruded by Carboniferous granitoids emplaced during the Variscan orogeny (Göncüoğlu et al., 2000; Ustaömer et al., 2012). The nature of the Karakaya Complex is debated but is generally considered a subduction-accretion complex associated with the Late Paleozoic–Early Mesozoic closure of the Paleotethys along the southern margin of Eurasia (Pickett and Robertson, 1996; Okay and Göncüoğlu, 2004; Federici et al., 2010; Ustaömer et al., 2016). The Karakaya Complex contains metamafic and metasedimentary rocks interpreted as seamounts of intra-oceanic basaltic composition and forearc basin and trench deposits (Pickett and Robertson, 1996) that were subsequently metamorphosed to blueschist and epidote-amphibolite with minor eclogite facies with estimated temperatures of  $340\text{--}550 \pm 50$  °C (Okay et al., 2002; Federici et al., 2010) with phengite, glaucophane, and barrosite Ar–Ar cooling dates around 200–215 Ma (Okay et al., 2002). The youngest Karakaya Complex units are unmetamorphosed or metamorphosed to zeolite to lower greenschist facies (120–376 °C) (Federici et al., 2010) and are unconformably overlain by Jurassic platform carbonates. The Cretaceous to present closure of the Neotethys and associated suturing is recorded in the Central Sakarya and Sarıcakaya Basins located north of the suture. Stratigraphic and paleocurrent (Oçakoğlu et al., 2018), provenance (Mueller et al., 2022; Campbell et al., 2023), and mudstone geochemistry records (Açıkalin et al., 2016) show the input of suture zone derived material into the Central Sakarya Basin from the Late Cretaceous through Eocene, interpreted as progressive suture zone uplift and exhumation during accretion and continental collision (Oçakoğlu et al., 2018; Okay et al., 2020; Mueller et al., 2022; Campbell et al., 2023). Cretaceous subduction-related arc volcanism and Paleogene syn-collisional volcanic centers are located within and to the north of the basins (Kasapoğlu et al., 2016; Ersoy et al., 2017, 2023; Keskin and Tüysüz, 2018). By Eocene times, increased plate coupling manifested as increased contractional deformation that partitioned the southern Central Sakarya Basin into the Sarıcakaya Basin (Mueller et al., 2022). The Eocene Sarıcakaya Basin received sediment from the suture zone and Karakaya Complex to the south and basement-involved thrust sheets to the north (Mueller et al., 2019).

## 4 Methods

### 4.1 Sample Information

Sedimentary samples were collected from Upper Cretaceous to Eocene siliciclastic sedimentary rocks of the Central Sakarya Basin and Sarıcakaya Basin in western Anatolia (Figure 2; Table S2). Detrital zircon U–Pb ages and Hf isotopes from these samples are already published (Mueller et al., 2019, 2022; Campbell et al., 2023); a set of 20 samples were chosen for detrital rutile U–Pb dating and trace element analysis. Heavy minerals were extracted using standard heavy mineral techniques, including crushing, water table, heavy liquid, and magnetic separation (Appendix A). Rutile grains were handpicked, rutile grains were picked from most samples, except for samples 16SKY26, 16SKY42 and 17OZK05 for which 260–320 grains were selected. Rutile grains were mounted in epoxy and polished





240 to expose the internal structure. Then, rutile mounts were carbon coated and imaged with a TFS Apreo-S with Lovac  
SEM with an energy-dispersive detector (EDS) to distinguish **TiO<sub>2</sub> grains from other heavy minerals** (Figure A1).

#### 4.2 U-Pb Analytical Protocol

Detrital rutile U-Pb geochronology was conducted at the Isotope Geochemistry Lab at the University of  
Kansas (KU-IGL) using a Thermo Element2 magnetic sector field ICP-MS coupled to a Photon Machines AnalyteG2  
245 excimer laser ablation system. The protocol was modified from Rösel et al. (2019) to optimize for low U contents  
(Appendix A; Table A2). The ICP-MS was manually tuned using NIST SRM 612 reference material glass to yield  
Th-U ratios close to 0.8 and low oxide production rates while maintaining high <sup>238</sup>U sensitivity. Grains were ablated  
for 25 seconds with a laser beam diameter of **50 μm** or fluence of 3.0 J/cm<sup>2</sup>, and **10 Hz** repetition rate. The  
secondary electron multiplier operated in both counting and analog modes ('both mode') to handle both the high U  
250 counts in the standards and low U counts in the unknowns. Primary and secondary reference materials were the **R10**  
(Luvizotto et al., 2009), Wodgina (Ewing, 2011), 9826J (Kylander-Clark, 2008), LJ04-08 (Apen et al., 2020), and  
Kragere (Kellett et al., 2018) standards, respectively. The data were reduced in iolite 4 (Paton et al., 2011), calibrated  
inst R10. The protocols reproduced the published ages of the reference materials to 5% or better (Figure A2). **Even**  
**with the modified protocol, a significant number of analyses did not meet quality control goals: 686 of 1,278 analyses**  
**255 were excluded due to anomalous (spiky) patterns in raw signal intensity** and a further 214 analyses were excluded for  
<sup>207</sup>Pb/<sup>206</sup>Pb error above 20%, leaving 378 analyses remaining (30%). Potential causes for these abnormal patterns and  
high Pb error include (1) elemental heterogeneity from ablating into small inclusions and/or lamellae; (2)  
inhomogeneities due to micro-cracks with different element/isotope composition; (3) heterogeneous amount of  
common lead incorporation during rutile growth; (4) textural and/or elemental heterogeneities due to multiple rutile  
260 growth events. Although, scenarios 3 and 4 are unlikely for Pb because it diffuses and should not cause spikes. Detrital  
rutile U-Pb raw data are given in the data repository (Mueller et al., 2023).

The SEM images do not give a clear picture of how to better select grains that will produce acceptable signal  
intensity and U-Pb concordance. Figure 3 shows SEM images of representative rutile grains after laser ablation. All  
grains appeared inclusion free before ablation, yet some analyses clearly ablated into inclusions (Figure 3C). Grains  
265 with clear inclusion lamellae yielded poor data quality (Figure 3B).

#### 4.3 Trace Element Geochemistry Analytical Protocol

Detrital rutile trace element geochemistry (<sup>49</sup>Ti, <sup>51</sup>V, <sup>53</sup>Cr, <sup>66</sup>Zn, <sup>69</sup>Ga, <sup>90</sup>Zr, <sup>93</sup>Nb, <sup>95</sup>Mo, <sup>118</sup>Sn, <sup>121</sup>Sb, <sup>177</sup>Hf,  
<sup>181</sup>Ta, <sup>182</sup>W) was conducted at the KU-IGL using the same instrumentation and parameters, except with a 25 or 35 μm  
spot size. Reference materials included **USGS GSD-IG and GS glasses and R10 rutile**. Trace element  
270 concentrations were calculated using the Trace Element routine in iolite 4 with <sup>49</sup>Ti as an internal standard; for rutile  
unknowns, TiO<sub>2</sub> was set to be 100 mass-% following U-Pb and trace element analysis mounts were imaged in an  
SEM at University of Nevada Reno (Figure 3). Most grains have both U-Pb and trace element results, but some grains  
have only U-Pb results due to the grain size being too small for a second ablation spot or have only trace element





275 results due to discarded U-Pb data. Detrital rutile trace element raw data are given in the data repository (Mueller et al., 2023).

## 5 U-Pb Results



### 5.1 Influence of Pb Corrections on Date Spectra

280 All the U-Pb results are displayed together in Figure 4 in Tera-Wasserburg space. A substantial number of analyses plot close to non-radiogenic common Pb values. This is evident in the convergence of data toward y-intercept values close to known common Pb values: from 1000 Ma to present, the  $^{207}\text{Pb}$ - $^{206}\text{Pb}_{\text{common}}$  ratio evolves from ~0.88 to 0.83 (Stacey and Kramers, 1975). Therefore, this section explores the sensitivity of U-Pb date spectra to  $^{208}\text{Pb}$ - and  $^{207}\text{Pb}$ -correction methods and to discordance filters in order to determine whether these factors change the overall provenance interpretations.

285 The uncorrected and corrected data are shown in Figure 5 as kernel density estimates (KDEs) and cumulative distributions. Resulting date distributions for each sample are shown in Figure A3, but due to small sample sizes, interpretations are based on the cumulative dataset. Within each common Pb correction method, the results are subdivided by concordance (see Figure 4). For the  $^{207}\text{Pb}$  corrections, concordance is defined in Tera-Wasserburg space. For the sake of comparison, the 100–40% concordant group for the  $^{208}\text{Pb}$  correction excludes the same grains that are  
290 categorized as 40–0% concordant in the  $^{207}\text{Pb}_{\text{ti}}$  correction. The 100–80%, 80–60%, and 60–40% concordance groups have modes centered around 95 Ma, 190 Ma, 310 Ma, and 580 Ma. The uncorrected,  $^{208}\text{Pb}$ -corrected with no concordance filter, and 40–0% concordance groups have broad date peaks with poorly defined date modes.

The different common Pb corrections produce differences in peak amplitude, the percent concordance has a larger impact on overall date distribution (Figure 5). The date difference between the  $^{207}\text{Pb}$ -corrected dates using  $t_{\text{i}}$   
295 and  $t_{208}$  is less than 1% for analyses less than 60% concordant and less than 5% for analyses 60–40% concordant (Figure 6). The difference in date significantly increases for grains that are less than 40% concordant. This result is replicated in statistical comparisons included in the data repository (i.e., similarity, likeness, cross-correlation, Kolmogorov-Smirnov; Mueller et al., 2023). For this reason, we prefer the date distributions that include all grains  
300 100–40% concordant, excluding grains below 40% concordant. However, the similarity in the  $^{207}\text{Pb}$  with  $t_{208}$  cumulative date distribution for the 100–40% and 40–0% groups is notable, which could warrant the inclusion of those low concordance grains. Ultimately, the prominent date modes are the same across  $^{207}\text{Pb}$ - and  $^{208}\text{Pb}$ -corrected groups, meaning that provenance interpretations are not affected by the choice of Pb correction method. This may not be the case for other datasets where the Pb correction method and concordance filter may influence the final date distribution and in cases where the KDE amplitude is important.



305 **5.2 Influence of Low-U Rutile on Age Spectra**

A common analytical workflow for detrital rutile is to first analyze trace elements then only collect U-Pb data on rutile above a given U concentration threshold (ca. > 4–5 ppm; Zack et al., 2004a; Okay et al., 2011; Rösel et al., 2019). Elemental concentrations are calculated based on the measured count rate (i.e., counts per second, CPS), which is inherently dependent on the individual mass spectrometer and laser ablation parameters (e.g., spot size, 310 fluence). The concentration in an unknown is calculated based on the known concentration in the primary reference material and measured CPS of the primary reference material. Hence, if sensitivity is increased or decreased proportionally for reference materials and unknowns across various ICP-MS instruments and analytical parameters, the resulting concentration (ppm) will be the same. Yet, for instruments with lower sensitivity, the signal background and counting statistics will require a higher CPS to achieve the same measured concentration (i.e., 4 ppm). In this way, 315 the U-threshold filter is instrument-dependent. The primary standard, R10, has a U concentration of 44 ppm (Luvizotto et al., 2009) and, in our measurements, on average, 2.1 million CPS  $^{238}\text{U}$ . The  $^{238}\text{U}$  baseline was about 5 CPS, therefore, the instrument set-up used here has a maximum detection limit of about 0.0003 ppm  $^{238}\text{U}$  (calculated from 3x background). The detrital rutile with the lowest uranium concentration (0.02 ppm) is nearly two orders of magnitude above this detection limit.

320 The U-threshold filter is intended to maximize the proportion of concordant rutile analyzed. This includes rutile that have low incorporation of U during growth (independent of analytical instrumentation) and rutile that have poorly resolved U-Pb ratios due to low U CPS such as old rutile and mafic rutile (machine dependent). This U-threshold filtering potentially introduces bias into the provenance results as omitting low-U rutile biases results toward younger and metapelitic sources. Therefore, we explore whether using a 4-ppm threshold rather than analyzing rutile 325 of all U concentrations is, in practice, best to maximize usable data or if it imparts a bias in provenance interpretations.

A comparison of analyzed rutile included with the U-threshold versus concordance filters is given in Figure 7. The U-threshold filter includes all grains with U higher than 4 ppm, whereas the concordance filter includes grains more than 40% concordant. Of the rutile that are more than 40% concordant, many have U concentrations below 4 ppm, and all are above 0.1 ppm. The majority of grains older than 250 Ma are above 4 ppm U. Thus, the U-threshold 330 filter does not seem to impart a bias toward older dates. The two filtering methods produce date spectra with the same dominant modes, yet the amplitude of peaks vary between methods. For example, the 190 Ma mode is more prominent with the concordance filter than with the U-threshold filter. Furthermore, the predominant date modes contain rutile of both metapelitic and metamafic origin (cf. next section and Figure 8). Even though the two filters do not yield different provenance interpretations in this case, most mafic-classified grains have U contents below 4 ppm and are in 335 the 190 Ma population. Hence, the U-threshold filter is likely biasing results toward pelitic sources. In this dataset, all grains more than 40% concordant are above 0.1 ppm, which could be a more suitable U-threshold. However, a significant number of highly discordant grains are also within 0.1 to 4 ppm U, meaning that the U threshold does not adequately delineate interpretable data. As the U-threshold filter is both instrumentation sensitivity dependent and biases provenance results, we suggest that a U-threshold protocol is not appropriate for provenance studies.



## 340 6 Trace Element Results

### 6.1 Source Lithology

Trace element results are provided in the supplementary information. Discrimination diagrams using V, Cr, Zr, Fe, and Nb can distinguish rutile from other TiO<sub>2</sub> polymorphs (Triebold et al., 2011), and all analyzed grains plot within the expected rutile fields (Appendix A; Figure A4). The Cr and Nb concentrations discriminate between  
345 metapelitic and metamafic source rocks (Zack et al., 2004a; Triebold et al., 2011, 2012). Even though the exact discrimination line between metamafic and metapelitic source lithologies is debated (e.g., Meinhold et al., 2008; Triebold et al., 2012), the detrital rutile in this dataset plot in both the metamafic and metapelitic fields (Figure 8).  
There is no clustering by sample or U-Pb date.

### 6.2 Source Metamorphism

The Zr-in-rutile temperature results are displayed alongside U concentration (Figure 9). In this dataset, Zr  
concentrations range from 2 to 1934 ppm, yielding a range in source rock minimum peak temperatures from 359 °C  
to 824 °C. Even though many studies only acquire U-Pb dates on rutile with U > 4–5 ppm, 87% of rutile in this study  
are below 4 ppm (n=517/592). This commonly accepted stratigraphic age has important implications for provenance  
interpretation. In our dataset, the majority of rutile with U > 4 ppm are classified as pelitic and generally have higher  
355 Zr contents (Figure 8 and Figure 9). Whereas low-U rutile in this study generally correlates with lower Zr contents  
(lower temperature) and includes the majority of mafic-classified grains (Figure 9). Therefore, the exclusion of low-  
U rutile in provenance studies likely misses sediment sourced from lower grade metamorphic units and metamafic  
sources.

The Zr-in-rutile thermometer generally preserves the crystallization or recrystallization temperature. The Zr-  
in-rutile thermometer can become uncoupled from the U-Pb age because Pb diffusion during metamorphic events or  
360 extended cooling periods will lead to partial or complete resetting of the U-Pb system (Cherniak et al., 2007; Luvizotto  
and Zack, 2009; Kooijman et al., 2012). When displayed in Tera-Wasserburg space, the 4 dominant modes—95 Ma,  
190 Ma, 310 Ma, 580 Ma—have fairly consistent Zr-in-rutile temperatures (Figure 10). The highest temperatures are  
found in the 95 Ma date mode, reaching granulite facies conditions. The 580 Ma and 310 Ma rutiles similarly preserve  
365 high temperatures, up to 700–800 °C, whereas the majority of 190 Ma rutiles show temperatures around 450–500 °C  
corresponding to blueschist/greenschist facies conditions. Because temperatures for the 190 Ma population are cooler  
than for the older events and are not high enough to have reset the U-Pb dates, we interpret these temperatures as  
primary. Furthermore, partially reset dates would smear the data along discordia from the initial crystallization event  
age, not towards common Pb.

### 370 6.3 Principal Component Analysis

Principal component analysis (PCA) was conducted on the detrital rutile trace element compositions (V, Cr, Zn, Ga, Zr, Nb, Mo, Sn, Sb, Hf, Ta, W) using OriginPro statistical software and the results are given in Appendix B. PCA is a multivariate statistical procedure that identifies the variables that explain the most amount of variance within



375 a dataset. The principal components are ranked based on the amount of variance they explain. Plots of principal component 'loadings' display the distribution of the trace element variables with respect to the principal components. Figure 11 shows that the variance between samples can largely be explained by Hf, Zr, Sn, Cr, V, Nb and Ta. Because Cr, Nb and Ta are protolith dependent (PC 2) and Hf and Zr are temperature dependent (PC 1), the variance in detrital rutile trace element chemistry is best explained by both protolith and metamorphic grade, allowing us to track these two properties of source rocks.

## 380 **7 Utility of Detrital Rutile Petrochronology**

### **7.1 Anatolian Sedimentary Provenance Interpretation**

Sedimentary provenance is interpreted from all detrital rutile dates together, rather than by sample, due to the small number of analyses in each (see Figure S3 for individual sample results). The detrital rutile results are displayed along with detrital zircon dates from the same Upper Cretaceous to Eocene units in the Central Sakarya and Sarıcakaya Basins (Figure 12; data from Campbell, 2017; Ocakoğlu et al., 2018; Mueller et al., 2019, 2022; Okay and Kylander-Clark, 2022). The rutile grains that define the ca. 95 Ma population (Figure 12) include some of the highest Zr-in-rutile temperatures (Figure 10) and are concurrent with a 110–76 Ma high flux magmatic event that is dominant in the detrital zircon record (Figure 12; Mueller et al., 2022). The lower plate Anatolide-Tauride northern margin underwent blueschist facies metamorphism in the Late Cretaceous, however, the sedimentary provenance record indicates no sediment transport across the suture zone between the Pontides and Anatolide-Tauride terranes in the latest Cretaceous (Okay and Kylander-Clark, 2022). Thus, the 95 Ma age population is interpreted as either igneous or metamorphic rutile from Late Cretaceous magmatism and associated contact metamorphism on the Pontides. The 190 Ma peak includes the lowest Zr-in-rutile temperatures (450–575 °C), mafic and pelitic sources, and predominantly low-U rutile. The age, lithology, and temperature findings support a Karakaya Complex sediment source. The Karakaya Complex contains intra-oceanic basalts and forearc deposits; the metamorphosed units reached temperatures of 340–550 °C around 200–215 Ma (Okay et al., 2002; Federici et al., 2010). Detrital zircons from Karakaya Complex units have age modes at ca. 235 Ma, 315 Ma, and 400 Ma interpreted as sediment input from the Pontides Triassic magmatic arc, Variscan granitoids, and crystalline basement to the forearc (Ustaömer et al., 2016). This 190 Ma rutile age population is not prominent in the detrital zircon spectra and records Karakaya Complex metamorphism. The 310 Ma and 580 Ma detrital rutile age populations are mirrored in the detrital zircon record and match the zircon age modes present in Pontides basement. The Carboniferous peak corresponds to a 330–340 Ma pulse of high-T metamorphism and 290–320 Ma magmatism during the Variscan orogeny (Ustaömer et al., 2012; Topuz et al., 2020). These basement units crop out along the thrust fault that partitions the two basins (Tuzaklı-Gümele Thrust; Figure 12b). Variscan-aged detrital rutiles were found in Jurassic sandstones in the Central Sakarya Basin and interpreted as derived from either primary Pontide basement or recycled sedimentary sources (Şengün et al., 2020). Therefore, the detrital rutile of this age in Upper Cretaceous to Eocene units could be derived from primary basement sources or recycled Jurassic sedimentary units. Notably the ca. 395 Ma peak in the detrital zircon record is absent from the rutile age spectra, possibly because the rutile of that age were overprinted by the Carboniferous high temperature event.



Scarce Silurian (440–420 Ma) and Devonian (400–380 Ma) metagneous rocks exist in the hanging wall of the  
410 Tuzaklı-Gümele Thrust (Topuz et al., 2020). The absence of this age population in the rutile record could be due to  
the scarcity of outcrops or sample size. Lastly, the 580 Ma Pan-African and older detrital rutile ages align with the  
detrital zircon age spectra. These grains could be sourced from the Pontides basement or recycled from sedimentary  
units (Ustaömer et al., 2012; Mueller et al., 2019); however, because grains of this age must have escaped any younger  
415 high-T events, we interpret them as polycyclic grains derived from recycled sedimentary units. Carboniferous and  
older zircon grains have been interpreted as a mix of primary crystalline Pontides basement and recycled sedimentary  
sources, including recycled from the Karakaya Complex metasedimentary units and from sedimentary units exposed  
along thrust sheets. Therefore, it is possible that the rutile grains are derived from primary sources or recycled from  
420 classic and younger sedimentary units. Together, the detrital zircon and rutile age spectra demonstrate that, from the  
Late Cretaceous to Eocene, sediment was sourced to the Central Sakarya and Sarıcakaya Basins from syn-depositional  
magmatic centers, the Karakaya Complex within the suture zone, the Pontides crystalline basement, and recycled  
sedimentary units.

## 7.2 Implications of New Workflow on Provenance Applications

Employing detrital rutile geochronology and geochemistry, and the workflows presented here, have several  
implications for the provenance interpretations. First, the various Pb correction methods produce similar age spectra  
425 and do not change the final provenance interpretations. Second, the 190 Ma population is poorly represented in the  
detrital zircon record (Figure 12). This means that detrital rutile is capturing a unique sedimentary provenance signal.  
The Karakaya Complex is not easily captured in the detrital zircon record due to both zircon-poor lithologies and the  
multi-cyclic Carboniferous and Devonian-aged grains. This finding emphasizes the utility of detrital rutile to  
discriminate between specific sediment sources. Third, the majority of rutile analyses in the 190 Ma group are low-U  
430 grains, meaning this age population would not have been captured using workflow protocols that filter out low U  
analyses (Figure 9). The Karakaya Complex is composed of metamafic and metapelitic rocks, and the rutile dataset  
demonstrates that low-U rutile are sourced from mafic and pelitic units (Figure 7 and Figure 8). The contribution of  
Karakaya Complex to the basin would be underrepresented without including low-U rutile. Additionally, the U  
threshold is dependent on the spot size and sensitivity of the ICP-MS used and does not adequately delineate  
435 interpretable data in a way that merits continued use. Lastly, the presence of 580 Ma grains means that those grains  
escaped younger high-T events, such as Variscan-related Carboniferous metamorphism (Figure 10). This supports the  
interpretation that the 580 Ma grains are recycled from sedimentary units, rather than derived from primary Pontide  
basement sources that underwent Carboniferous metamorphism. In this way, paired rutile U-Pb dates and Zr-in-rutile  
thermometry can discriminate between potential sediment sources.

440 Because detrital rutile is capturing sediment input from a terrane not represented in the zircon record, detrital  
rutile has the potential to close the gap between the advances in zircon applicability and its limitations. For example,  
detrital zircon U-Pb dating, (U-Th)/He and fission track thermochronometry, and trace element and isotopic  
geochemistry are being performed on single grains to reconstruct the timing, tempo, and spatial extent of  
sedimentation, magmatism, deformation, exhumation, and crustal thickness. Rutile provides the opportunity to answer



445 similar orogenic-scale questions in areas where zircon alone is insufficient. The dataset from Anatolia demonstrates  
that detrital rutile provides information on sedimentation, deformation, and metamorphism. Finally, the accretion and  
collision of subduction complexes and oceanic plateaus has been notoriously difficult to discern with provenance  
techniques, often inferred from the absence of detrital zircon age modes (Shekut and Licht, 2020; Darin et al., 2022).  
This work shows that detrital rutile is a promising proxy to track sediment input from accreted terranes and can be  
450 applied to convergent margins worldwide.

## 8 Conclusion

Sedimentary provenance analysis plays a crucial role in understanding the geodynamic, magmatic, structural,  
and topographic evolution of convergent margins. Detrital zircon U-Pb geochronology is a widely used technique,  
however, it has several limitations and can struggle to capture significant events in a convergent margin lifecycle (e.g.,  
455 low grade metamorphism, mafic protoliths). Detrital rutile provides one opportunity to overcome these limitations.  
This study provides methods for using detrital rutile U-Pb and trace element analysis in tracking sediment input from  
metamorphic units using a new dataset from the Central Sakarya and Sarıcakaya Basins in Anatolia. We present a  
workflow for evaluating discordance and common Pb, which is critical for confidently interpreting age distributions.  
The results show that common Pb correction is important, but the choice of correction method is less influential, and  
460 that grains up to 60% discordant can be used for meaningful provenance interpretation. Using a concordance filter is  
more appropriate than filtering out low-U rutile. Low-U rutile comprise an important detrital population—lower grade  
metamorphic units and metamafic sources—that would otherwise be missed with analytical protocols that screen U  
concentration. Based on trace element geochemistry, these low-U rutile grains are classified as metamafic and  
metapelitic and predominantly have greenschist-blueschist Zr-in-rutile temperatures, thus correspond to sediment  
465 input from the subduction accretion Karakaya Complex. Sedimentary provenance from the Karakaya Complex is  
poorly resolved in the detrital zircon record, further highlighting the potential of detrital rutile as an important  
provenance proxy in orogenic settings.

## Appendix A: Sample Preparation and Analytical Methods

### A.1 Sample Preparation

470 The samples in this study were previously separated for detrital zircon analysis (Table A1; Mueller et al.,  
2022, 2019). In order to extract detrital rutile, all heavy mineral fractions from post-water table separation steps were  
recombined and reprocessed. Then, samples were separated in heavy liquids (i.e., methylene iodide). The Frantz  
magnetic separator was set to 20° side slope and 20° forward slope such that rutile grains were separated into the 0.7  
to 1.5 amp. fraction (Rosenblum and Brownfield, 2000). Rutile grains were handpicked with a Leica M205C binocular  
475 microscope using transmitted and polarized light. For samples with a small quantity of heavy mineral grains, rutile  
was picked from all 0.3 to >1.5 amp. magnetic fractions. Rutile grains were red-brown-yellow color in reflected light,  
red to opaque in plane polarized light, and displayed a resinous to vitreous luster; grains were well rounded to euhedral  
with many displaying twinning characteristic of rutile's tetragonal crystal system and striations parallel to the long



axis. Grains were placed on Kapton tape and mounted in epoxy in 25-mm diameter cups. The mounts were polished  
480 to expose the internal structure of the grains.

Rutile mounts were carbon coated and imaged with a TFS Apreo-S with Lovac SEM with an energy-dispersive detector (EDS) to distinguish rutile grains from other spurious heavy minerals (Figure A1). Then the epoxy mounts were polished with 1  $\mu\text{m}$  and 0.25  $\mu\text{m}$  grit in felt. Mounts were soaked in 2M nitric acid ( $\text{HNO}_3$ ) in the ultrasonic, then in ultra-pure water in the ultrasonic to remove carbon coat remnants.

#### 485 **A.2 U-Pb Geochronology**

Detrital rutile U-Pb geochronology was conducted at the Isotope Geochemistry Lab at the University of Kansas using a Thermo Element2 magnetic sector field ICP-MS coupled to a Photon Machines AnalyteG2 excimer laser ablation system (see also metadata in Table A2). We used a modified protocol from Rösel et al. (2019), which we optimized for low U concentrations. Because metamafic rocks, which have low U concentrations, were suspected  
490 to be an important sedimentary source, we designed a protocol to maximize U sensitivity. We spent a significant amount of time tuning acquisition parameters and opted for a laser beam diameter of 50  $\mu\text{m}$ , running the secondary electron multiplier in ‘both mode’ to handle both the high U counts in the standards and low U counts in the unknowns, and using a long washout time of 15 seconds time to get a steady, low  $^{238}\text{U}$  background. Rutile unknowns were calibrated against a suite of reference materials. The data were reduced in *iolite 4* (Paton et al., 2011), calibrated  
495 against the R10 standard. Individual analyses with >20% discordance in  $^{207}\text{Pb}/^{206}\text{Pb}$  ratios (more lenient than the 15% recommended in Lippert, 2014) or abnormal patterns in raw signal intensity were excluded from analyses and interpretations.

The accuracy of the protocol was evaluated using a suite of international standards. We used R10 as the primary standard (1091.6  $\pm$  3.5 Ma TIMS age; Luvizotto et al., 2009), and the secondary standards included Wodgina  
500 (2845.8  $\pm$  7.8 Ma TIMS age; Ewing, 2011), Kragerø (1085.7  $\pm$  7.9 Ma TIMS age; Kellett et al., 2018), 9826J (381.9  $\pm$  1.1 Ma TIMS age; Kylander-Clark, 2008), and LJ04-08 (498  $\pm$  3 Ma LA-ICP-MS age; Apen et al., 2020). Figure A2 displays the weighted mean of the uncorrected and corrected ages as the percent deviation from the published age (see also the data repository Mueller et al., 2023). The rutile U-Pb dates of individual sample are shown as histograms in Figure A3.

#### 505 **A.3 Trace Element Geochemistry**

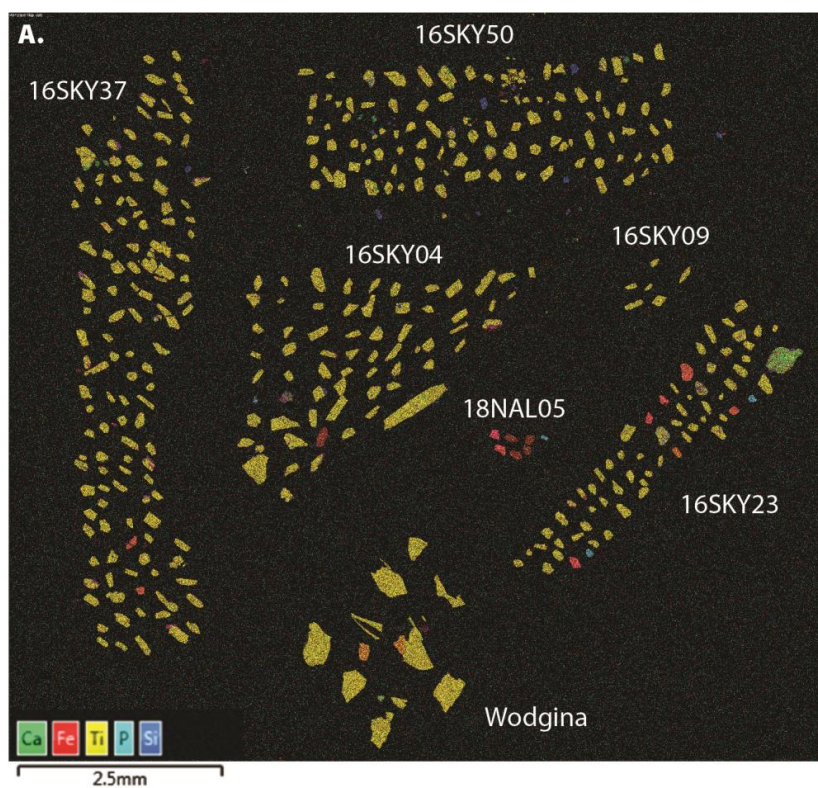
Detrital rutile trace element geochemistry was conducted at the Isotope Geochemistry Lab at the University of Kansas using a Thermo Element2 magnetic sector field ICP-MS coupled to a Photon Machines AnalyteG2 excimer laser ablation system (see also Table A2). Trace elements ( $^{49}\text{Ti}$ ,  $^{51}\text{V}$ ,  $^{53}\text{Cr}$ ,  $^{66}\text{Zn}$ ,  $^{69}\text{Ga}$ ,  $^{90}\text{Zr}$ ,  $^{93}\text{Nb}$ ,  $^{95}\text{Mo}$ ,  $^{118}\text{Sn}$ ,  $^{121}\text{Sb}$ ,  $^{177}\text{Hf}$ ,  $^{181}\text{Ta}$ ,  $^{182}\text{W}$ ) were determined by ablating material from a 25–35  $\mu\text{m}$  laser beam diameter with a beam energy  
510 density of 3.0 J/cm<sup>2</sup> and a repetition rate of 10 Hz. Trace element reference materials included USGS GSD-1G and USGS GSC-1G glasses (Jochum et al., 2011) and R10 rutile (Luvizotto et al., 2009). Trace element concentrations were calculated using the Trace Element routine in *iolite 4* (Paton et al., 2011) with  $^{49}\text{Ti}$  as an internal standard; for





rutile unknowns, TiO<sub>2</sub> was set to be 100 mass-%. Following U-Pb and trace element analysis mounts were imaged in a SEM at University of Nevada Reno.

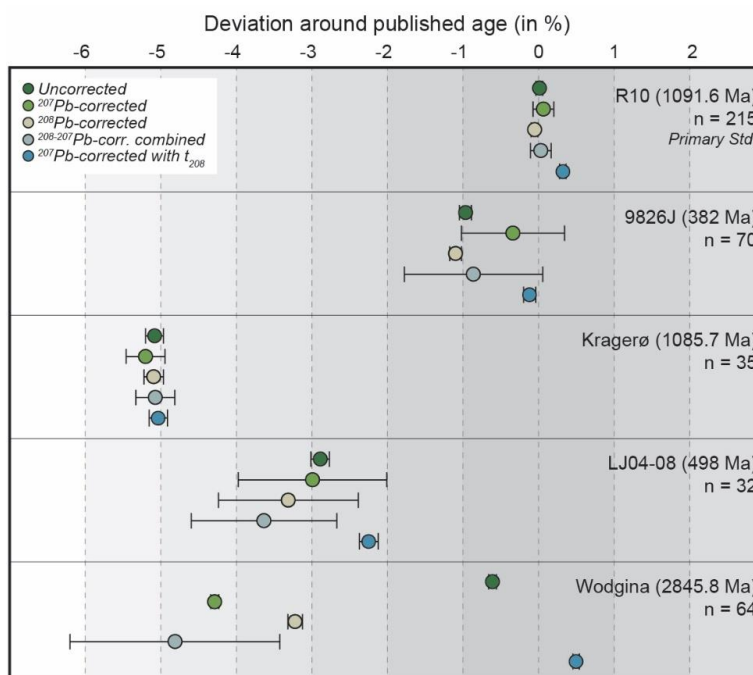
515 Trace element composition was then used to confirm that the analyzed grains are rutile. TiO<sub>2</sub> polymorphs rutile, brookite and anatase are argued to be optically distinct (Mange and Maurer, 1992) or optically indistinguishable (Triebold et al., 2011). Either way, V, Cr, Zr, Fe, and Nb concentrations vary systematically among TiO<sub>2</sub> polymorphs (Triebold et al., 2011). Discrimination diagrams of Cr versus V and V versus Zr can verify that analyzed grains are rutile. The grains from this study are plotted alongside the polymorph dataset of Triebold et al. (2011) which were  
520 classified using Raman spectrometry (Figure A4). All samples from this study plot within the range of rutile grains.





525

**Figure A1. SEM EDS imaging of rutile grain mount 21RtF. (A) EDS elemental map where grains are colored by elements Ca, Fe, Ti, P, and Si. Rutile ( $\text{TiO}_2$ ) grains are yellow, iron oxides are red, zircon are blue, and apatite are green. (B) Typical spectra of a rutile grain.**



530 **Figure A2.** Deviation around the published age for the primary and secondary rutile reference materials. Circles and horizontal bars correspond to the weighted mean and standard deviation for analyses over all sessions. The various correction methods are explained in the main text. Note: The final iteration of the  $^{208}\text{Pb}$  correction yields a corrected  $^{238}\text{U}/^{206}\text{Pb}$  ratio. The combined  $^{208-207}\text{Pb}$  correction follows the  $^{207}\text{Pb}$  correction method in Tera-Wasserburg space using the new  $^{208}\text{Pb}$ -corrected  $^{238}\text{U}/^{206}\text{Pb}$  ratio and the original  $^{207}\text{Pb}/^{206}\text{Pb}$  ratio. In general, this combined correction method performed poorly and was not applied to detrital unknowns. Data from the figure are included in the data repository.

535

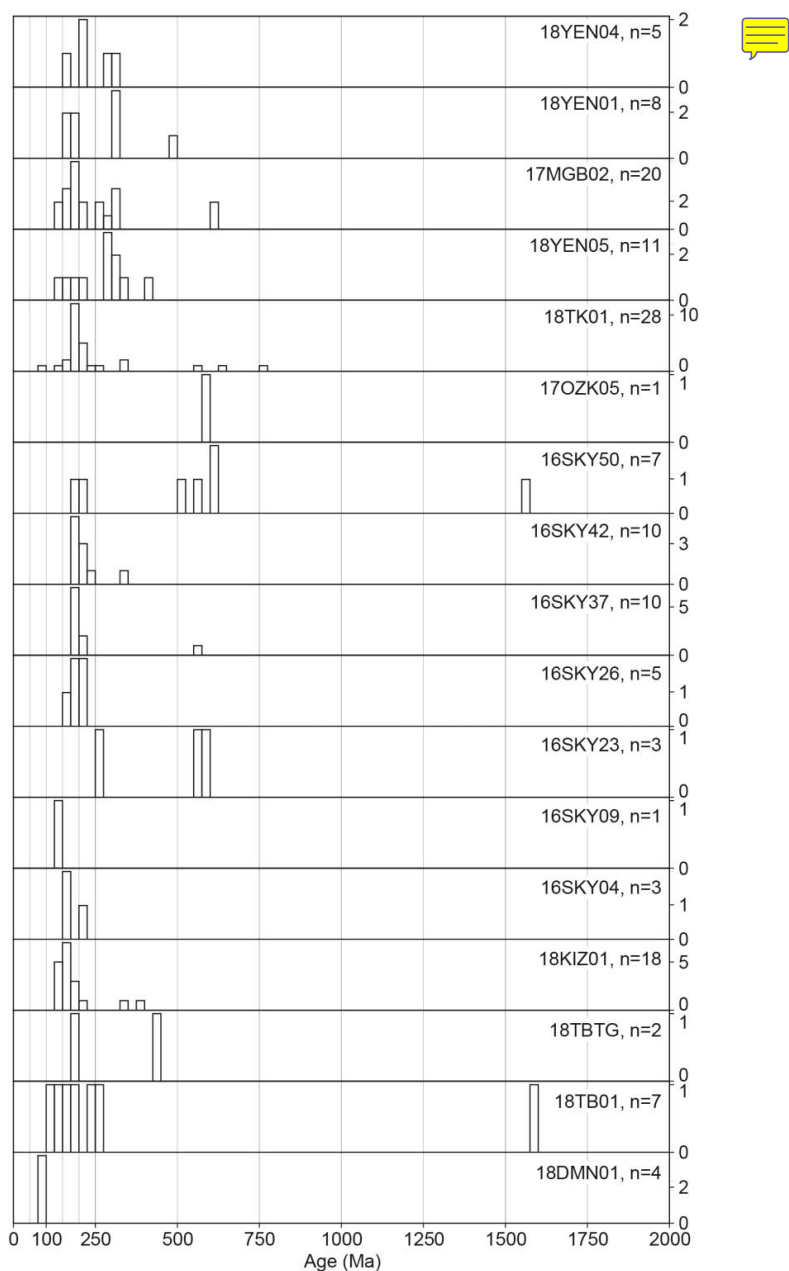
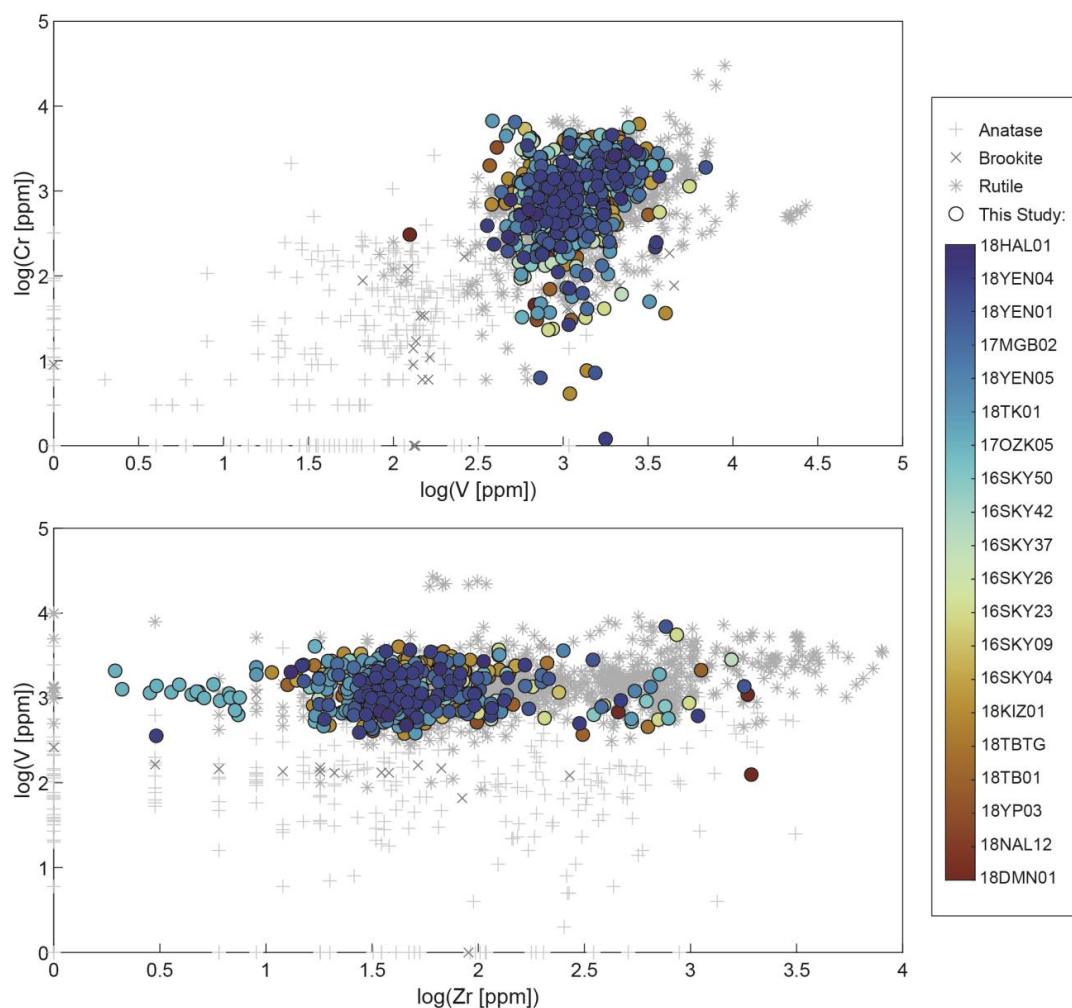


Figure A3. Histograms of detrital rutile U-Pb ages by sample. Histograms are 25 Myr bins and the ages shown are the  $^{207}\text{Pb}$  correction with  $t_{208}$ . Visualized with detritalPy (Sharman et al., 2018).



540

**Figure A4.** TiO<sub>2</sub> polymorph discrimination diagrams using (a) Cr versus V and (b) V versus Zr concentrations of analyzed grains. Rutile grains from this study, colored by sample, plot within the range of rutile grains identified in Triebold et al. (2011).

545



**Table A1. Sample Information. IGSN: International Geo Sample Number, CSB: Central Sakarya Basin, SB: Sarıcakaya Basin. CSB and SB stratigraphic sections are from Ocakoglu et al. (2018) and Mueller et al. (2019), respectively.**



Sample Name	IGSN	Unit	Basin and Section	Stratigraphic Age	Latitude	Longitude	Sample and detrital zircon source
18DMN01	10.58052/IEMUE0005	Değirmenözü Fm	CSB, Okçular Section	Santonian	40.373917	30.977778	Mueller et al., 2022
18NAL12	10.58052/IEMUE000J	Yenipazar Fm	CSB, Nallihan Section	Up. Camp.–Maastrichtian	40.245028	31.309472	Mueller et al., 2022
18TK01	10.58052/IEMUE000I	Çataltepe Fm	CSB, Taraklı Section	Paleocene–lower Eocene	40.327833	30.520861	Mueller et al., 2022
18KIZ01	10.58052/IEMUE000C	Kızılçay Fm	CSB, Okçular Section	Paleocene–lower Eocene	40.396667	30.962861	Mueller et al., 2022
18YEN05	10.58052/IEMUE000D	Kızılçay Fm	CSB, Yenipazar Section	Paleocene–lower Eocene	40.189639	30.626167	Mueller et al., 2022
18TB01	10.58052/IEMUE000F	Taraklı Fm	CSB, Taraklı Section	Paleocene–lower Eocene	40.357556	30.524444	Mueller et al., 2022
18TBTG	10.58052/IEMUE000G	Taraklı Fm	CSB, Taraklı Section	Paleocene–lower Eocene	40.355111	30.522278	Mueller et al., 2022
18YPO3	10.58052/IEMUE000K	Yenipazar Fm	CSB, Okçular Section	Lower Paleocene	40.389556	30.990306	Mueller et al., 2022
16SKY04	10.58052/IEMUE0017	Mihalgazi Fm	SB, Mayıslar Section	Ypresian	40.030250	30.652306	Mueller et al., 2019
16SKY09	10.58052/IEMUE0019	Mihalgazi Fm	SB, Mayıslar Section	Ypresian–Lutetian	40.033250	30.651222	Mueller et al., 2019
16SKY23	10.58052/IEMUE001H	Mihalgazi Fm	SB, Iğdir Section	Ypresian	40.057806	30.686833	Mueller et al., 2019
16SKY26	10.58052/IEMUE001K	Mihalgazi Fm	SB, Iğdir Section	Ypresian–Lutetian	40.058583	30.688083	Mueller et al., 2019
16SKY37	10.58052/IEMUE001Q	Mihalgazi Fm	SB, Kapıkaya Section	Ypresian–Lutetian	40.072889	30.741806	Mueller et al., 2019
16SKY42	10.58052/IEMUE001T	Mihalgazi Fm	SB, Kapıkaya Section	Ypresian–Lutetian	40.074500	30.743944	Mueller et al., 2019
16SKY50	10.58052/IEMUE001W	Mihalgazi Fm	SB, Kapıkaya Section	Ypresian–Lutetian	40.078639	30.744722	Mueller et al., 2019
17OZK05	10.58052/IEMUE001Z	Mihalgazi Fm	SB, Ozanköy Section	Ypresian–Lutetian	40.138917	30.931111	Mueller et al., 2019
17MGB02	10.58052/IEMUE0007	Gemiciköy Fm	CSB, Yenipazar Section	Up. Lutetian–Low. Bartonian	40.210444	30.615528	Mueller et al., 2022
18YEN01	10.58052/IEMUE0008	Gemiciköy Fm	CSB, Yenipazar Section	Upper Bartonian–Priabonian	40.251000	30.534750	Mueller et al., 2022
18YEN04	10.58052/IEMUE0009	Güvenç Fm	CSB, Yenipazar Section	Lutetian	40.193583	30.623028	Mueller et al., 2022
18HAL01	10.58052/IEMUE000A	Halidiye Fm	CSB, Okçular Section	Lutetian	40.396889	30.960694	Mueller et al., 2022



550 Table A2. University of Kansas Isotope Geochemistry Lab LA-ICP-MS Metadata

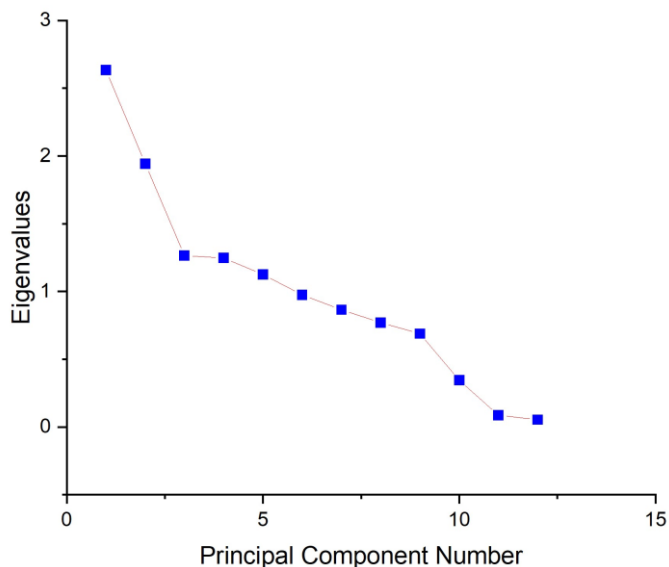
<b>Laboratory and Sample Preparation</b>	
Laboratory name	The University of Kansas, Dept. of Geology, Isotope Geochemistry Lab
Sample type/mineral	Rutile
Sample preparation	1-in epoxy rounds
Imaging	EDS in SEM
<b>Laser Ablation System</b>	
Make, model & type	ATL ArF excimer laser (193 nm), Photon Machines AnalyteG2
Ablation cell & volume	HeLex 9-sample cell
Laser wavelength	193 nm
Pulse width (ns)	5 ns
Fluence	3.0 J/cm <sup>2</sup> (77% at 5mJ output)
Repetition rate	10 Hz
Spot size (um)	Trace elements: 25 μm; U-Pb: 50 μm
Sampling mode / pattern	Single spots
Carrier gas	He, 1.1 l/min, Ar, 1.07 l/min
Ablation duration	25s
Cell carrier gas flow	He, 1.1 l/min
<b>ICP-MS Instrument</b>	
Make, Model & type	Thermo Element2 magnetic sector field ICP-MS (single collector)
Sample introduction	Aerosol with sample + He was mixed with Ar using a T-connector 15 cm upstream from torch
RF power	1200–1250 W
Make-up gas flow	Ar, 1.07 l/min
Sampling depth	ca. 20 μm
Detection system	single detector (SEM), counting & analog modes
Elements/ isotopes analyzed	Trace elements: 49Ti, 51V, 53Cr, 56Fe, 66Zn, 69Ga, 90Zr, 93Nb, 95Mo, 118Sn, 121Sb, 177Hf, 181Ta, 182W. U-Pb: 206Pb, 207Pb, 208Pb, 232Th, 238U
Integration time per channel (Sample Time)	Trace elements: 49Ti=3 ms, 90Zr=20 ms, and 10 ms for all other isotopes; U-Pb: 206=8 ms, 207=10 ms, 208=2 ms, 232=2 ms, 238=4 ms
Total integration time (Segment Duration)	Trace elements: 49Ti=9 ms, 90Zr=20 ms, and 10 ms for all other isotopes; U-Pb: 206Pb=32 ms, 207Pb=40 ms, 208Pb=8 ms, 232Th=8 ms, 238U=20 ms
Total method time	Trace elements: 40s (120 runs, 1 pass); U-Pb: 31s (100 runs, 3 passes)
ICP Dead time	6 ns
UO <sup>+</sup> /U <sup>+</sup>	≤0.25%
232Th <sup>+</sup> /238U <sup>+</sup>	>0.75
<b>Data Processing</b>	
Gas blank	Trace elements: 7–15 s, U-Pb: 7–15 s
Calibration strategy	Trace elements: standard-sampling bracketing + internal standardization assuming 100% TiO <sub>2</sub> ; U-Pb: standard-sampling bracketing
Reference material info	Trace elements: GSD-1G (Guillong et al., 2005; Jochum et al., 2005); U-Pb: R10 (Luvizotto et al., 2009)
Internal std for trace elements	49Ti





Data processing package used / Correction for LIEF	Iolite 4 (Paton et al., 2011): Trace elements: Trace Elements data reduction scheme; U-Pb: U-Pb Geochronology data reduction scheme; exponential LIEF correction for U-Pb ratios.
Common-Pb correction, composition and uncertainty	See text for discussion.
Uncertainty level & propagation	Trace elements: 2se internal uncertainty; U:Pb: 2se propagated uncertainty from U-Pb Geochronology data reduction scheme. Concordia diagrams were plotted using IsoplotR (Vermeesch, 2018) with 2s uncertainty ellipses
Reproducibility	Trace elements: 5–7%. U-Pb ratios: 2–4%
Quality control / Validation	Trace elements: R10 (Luvizotto et al., 2009) and GSC-1G (Guillong et al., 2005; Jochum et al., 2005); U-Pb: Wodgina (Ewing, 2011), Kragerø (Kellett et al., 2018), 9826J (Kylander-Clark, 2008), LJ04-08 (Apen et al., 2020)

### Appendix B: Additional Principal Component Analysis Information



555 **Figure B1.** Principal component analysis scree plot displaying the eigenvalues for each principal component. Data are in Table B2.

**Table B1.** Principal Component Analysis – Correlation Matrix

10	V	Cr	Zn	Ga	Zr	Nb	Mo	Sn	Sb	Hf	Ta	W
V	1	0.28702	0.08471	-0.00424	0.05335	-0.09225	-0.04913	0.30235	-0.10058	0.14697	-0.06449	0.11768
Cr	0.28702	1	0.00721	-0.06293	-0.02758	-0.14992	-0.0576	0.13129	-0.11661	0.02323	-0.18616	0.02185
Zn	0.08471	0.00721	1	0.20306	-6.68E-04	-0.06795	0.00211	0.10389	-0.02017	-0.02065	-0.07042	-0.01978
Ga	-0.00424	-0.06293	0.20306	1	0.02637	-0.01569	-0.0019	0.11868	-0.00756	0.03545	-0.02975	0.04133



<b>Zr</b>	0.05335	-0.02758	-6.68E-04	0.02637	1	0.14416	0.23746	3.63E-01	-0.02579	0.93181	0.13945	0.17929
<b>Nb</b>	-0.09225	-0.14992	-0.06795	-0.01569	0.14416	1	-0.00703	0.14644	0.06101	0.15243	0.90801	0.13124
<b>Mo</b>	-0.04913	-0.0576	0.00211	-0.0019	0.23746	-0.00703	1	0.45606	-0.01226	0.14038	-0.02039	0.11896
<b>Sn</b>	0.30235	0.13129	0.10389	0.11868	3.63E-01	0.14644	0.45606	1	0.11909	0.35819	0.15676	0.23521
<b>Sb</b>	-0.10058	-0.11661	-0.02017	-0.00756	-0.02579	0.06101	-0.01226	0.11909	1	-0.03755	0.09806	0.06319
<b>Hf</b>	0.14697	0.02323	-0.02065	0.03545	0.93181	0.15243	0.14038	0.35819	-0.03755	1	0.13769	0.26427
<b>Ta</b>	-0.06449	-0.18616	-0.07042	-0.02975	0.13945	0.90801	-0.02039	0.15676	0.09806	0.13769	1	0.06838
<b>W</b>	0.11768	0.02185	-0.01978	0.04133	0.17929	0.13124	0.11896	0.23521	0.06319	0.26427	0.06838	1

560 **Table B2. Principal Component Analysis – Eigenvalues of the Correlation Matrix**

	<b>Eigenvalue</b>	<b>Percentage of Variance</b>	<b>Cumulative</b>
<b>1</b>	2.63379	21.95%	21.95%
<b>2</b>	1.94337	16.19%	38.14%
<b>3</b>	1.26467	10.54%	48.68%
<b>4</b>	1.24705	10.39%	59.07%
<b>5</b>	1.12556	9.38%	68.45%
<b>6</b>	0.97551	8.13%	76.58%
<b>7</b>	0.86476	7.21%	83.79%
<b>8</b>	0.77053	6.42%	90.21%
<b>9</b>	0.68894	5.74%	95.95%
<b>10</b>	0.345	2.87%	98.83%
<b>11</b>	0.0868	0.72%	99.55%
<b>12</b>	0.05402	0.45%	100.00%

**Table B3. Principal Component Analysis – Extracted Eigenvectors**

	<b>Coefficients of PC1</b>	<b>Coefficients of PC2</b>	<b>Coefficients of PC3</b>	<b>Coefficients of PC4</b>	<b>Coefficients of PC5</b>
<b>V</b>	0.11188	0.32574	0.5509	0.18163	0.00963
<b>Cr</b>	-0.02241	0.33015	0.54321	-0.00609	0.08221
<b>Zn</b>	0.00128	0.1495	-0.09679	0.56211	-0.35561
<b>Ga</b>	0.04679	0.07679	-0.24684	0.52186	-0.39737
<b>Zr</b>	0.49771	0.16248	-0.18544	-0.30947	-0.25365
<b>Nb</b>	0.3141	-0.54281	0.24962	0.12009	-0.0531
<b>Mo</b>	0.24009	0.15855	-0.34487	0.10349	0.48557
<b>Sn</b>	0.40793	0.20734	0.04078	0.32142	0.3218
<b>Sb</b>	0.04322	-0.15434	-0.20528	0.19598	0.42865
<b>Hf</b>	0.50092	0.18027	-0.08342	-0.30607	-0.28105
<b>Ta</b>	0.30613	-0.55267	0.24494	0.12582	-0.0438
<b>W</b>	0.2605	0.07567	0.06886	0.08088	0.19405



#### 565 **Data availability**

The detrital rutile trace element and U-Pb raw data, results and Pb correction methods; rutile U-Pb reference material raw data and results; and statistical comparison of Pb correction methods are stored in an Open Science Framework data repository that can be accessed at <https://doi.org/10.17605/OSF.IO/A4YE5> (Mueller et al., 2023). Analyses and plots were performed in MATLAB (The MathWorks Inc., 2021).

#### 570 **Author contributions**

MAM conceptualized the project; MAM and AM performed the formal data analysis; MAM and AL acquired funding; all authors were involved in the investigation; MAM, AL, and AM developed the methodology; MAM and AM performed the validation; MAM completed the data visualizations; MAM wrote the original draft; all authors reviewed and edited the manuscript.

#### 575 **Competing interests**

The authors declare that they have no conflict of interest.

#### **Disclaimer**

Publisher's note: Copernicus Publications remains neutral with regard to jurisdictional claims in published maps and institutional affiliations.

#### 580 **Acknowledgements**

We thank Çelik Ocakoğlu, Jan Westerweel, Kate Huntington, Alison Duvall, Sean Mulcahy, Scott Braswell, Joel DesOrmeau, Scott Dakins, and Eric Steig for support in the field and lab. We thank Andrew Kylander-Clark, Francisco Apen, and Peter Downes for reference materials and Margo Odlum and Eirini Poulaki for discussions on U-Pb data reduction. We thank the *iolite* team for student access.

#### 585 **Financial support**

This work was funded by the University of Washington Department of Earth and Space Sciences and NSF EAR-1543684 and EAR-2141115.



## References

- Açikalın, S., Ocakoğlu, F., Yılmaz, İ. Ö., Vonhof, H., Hakyemez, A., and Smit, J.: Stable isotopes and geochemistry of a  
590 Campanian–Maastrichtian pelagic succession, Mudurnu–Göynük Basin, NW Turkey: Implications for palaeoceanography,  
palaeoclimate and sea-level fluctuations, *Palaeogeogr. Palaeoclimatol. Palaeoecol.*, 441, 453–466,  
<https://doi.org/10.1016/j.palaeo.2015.10.005>, 2016.
- Aksay, A., Pehlivan, Ş., Gedik, I., Bilginer, E., Duru, M., Akbaş, B., and Altun, I.: Geologic map of Turkey (Zonguldak, Scale  
1:500,000), Maden Tetkik ve Arma Genel Müdürlüğü, Ankara, Turkey, 2002.
- 595 Apen, F. E., Rudnick, R. L., Cottle, J. M., Kylander-Clark, A. R. C., Blondes, M. S., Piccoli, P. M., and Seward, G.: Four-  
dimensional thermal evolution of the East African Orogen: accessory phase petrochronology of crustal profiles through the  
Tanzanian Craton and Mozambique Belt, northeastern Tanzania, *Contrib. Mineral. Petrol.*, 175, 97,  
<https://doi.org/10.1007/s00410-020-01737-6>, 2020.
- Blum, M. and Pecha, M.: Mid-Cretaceous to Paleocene North American drainage reorganization from detrital zircons,  
600 *Geology*, 42, 607–610, <https://doi.org/10.1130/G35513.1>, 2014.
- Bracciali, L., Parrish, R. R., Horstwood, M. S. A., Condon, D. J., and Najman, Y.: UPb LA-(MC)-ICP-MS dating of rutile:  
New reference materials and applications to sedimentary provenance, *Chem. Geol.*, 347, 82–101,  
<https://doi.org/10.1016/j.chemgeo.2013.03.013>, 2013.
- Campbell, C. F.: Tectonic Evolution of the Izmir-Ankara Suture Zone in Northwest Turkey using Zircon U-Pb Geochronology  
605 and Zircon Lu-Hf Isotopic Tracers, M.S., University of Kansas, United States -- Kansas, 99 pp., 2017.
- Campbell, C. F., Mueller, M. A., Taylor, M. H., Ocakoğlu, F., Möller, A., Métais, G., Coster, P. M. C., Beard, K. C., and Licht,  
A.: The Geodynamic Implications of Passive Margin Subduction in Northwest Turkey, *Geochem. Geophys. Geosystems*, 24,  
e2022GC010481, <https://doi.org/10.1029/2022GC010481>, 2023.
- Carrapa, B.: Resolving tectonic problems by dating detrital minerals, *Geology*, 38, 191–192,  
610 <https://doi.org/10.1130/focus022010.1>, 2010.
- Cherniak, D. J., Manchester, J., and Watson, E. B.: Zr and Hf diffusion in rutile, *Earth Planet. Sci. Lett.*, 261, 267–279,  
<https://doi.org/10.1016/j.epsl.2007.06.027>, 2007.
- Chew, D., O’Sullivan, G., Caracciolo, L., Mark, C., and Tyrrell, S.: Sourcing the sand: Accessory mineral fertility, analytical  
and other biases in detrital U-Pb provenance analysis, *Earth-Sci. Rev.*, 202, 103093,  
615 <https://doi.org/10.1016/j.earscirev.2020.103093>, 2020.
- Chew, D. M., Sylvester, P. J., and Tubrett, M. N.: U–Pb and Th–Pb dating of apatite by LA-ICPMS, *Chem. Geol.*, 280, 200–  
216, <https://doi.org/10.1016/j.chemgeo.2010.11.010>, 2011.
- Clift, P. D., Hodges, K. V., Heslop, D., Hannigan, R., Van Long, H., and Calves, G.: Correlation of Himalayan exhumation  
rates and Asian monsoon intensity, *Nat. Geosci.*, 1, 875–880, <https://doi.org/10.1038/ngeo351>, 2008.
- 620 Cramer, F., Shephard, G. E., and Heron, P. J.: The misuse of colour in science communication, *Nat. Commun.*, 11, 5444,  
<https://doi.org/10.1038/s41467-020-19160-7>, 2020.
- Darin, M. H., Armentrout, J. M., and Dorsey, R. J.: Oligocene onset of uplift and inversion of the Cascadia forearc basin,  
southern Oregon Coast Range, USA, *Geology*, <https://doi.org/10.1130/G49925.1>, 2022.



Dickinson, W. R.: Plate tectonics and sedimentation, *Soc. Econ. Paleontol. Mineral. Spec. Publ.*, 22, 1–27, 1974.

625 Dickinson, W. R. and Suczek, C. A.: Plate Tectonics and Sandstone Compositions, *AAPG Bull.*, 63, 2164–2182, 1979.

Ersoy, E. Y., Akal, C., Genç, Ş. C., Candan, O., Palmer, M. R., Prelević, D., Uysal, İ., and Mertz-Kraus, R.: U-Pb zircon geochronology of the Paleogene – Neogene volcanism in the NW Anatolia: Its implications for the Late Mesozoic-Cenozoic geodynamic evolution of the Aegean, *Tectonophysics*, 717, 284–301, <https://doi.org/10.1016/j.tecto.2017.08.016>, 2017.

630 Ersoy, E. Y., Akal, C., Palmer, M. R., and Mertz-Kraus, R.: U-Pb dating of arc to post-collisional magmatic events in northwestern Anatolia: The Eocene Granitoids in NW Anatolia revisited, *J. Asian Earth Sci.* X, 9, 100148, <https://doi.org/10.1016/j.jaesx.2023.100148>, 2023.

Ewing, T. A.: Hf isotope analysis and U-Pb geochronology of rutile : technique development and application to a lower crustal section (Ivrea-Verbano Zone, Italy), <https://doi.org/10.25911/5d74e68841e8d>, 2011.

Faure, G.: *Principles of Isotope Geology*, 2nd Edition., Wiley & Sons, Inc., 608 pp., 1986.

635 Federici, I., CAVAZZA, W., OKAY, A. I., BEYSSAC, O., ZATTIN, M., CORRADO, S., and DELLISANTI, F.: Thermal Evolution of the Permo–Triassic Karakaya Subduction-accretion Complex between the Biga Peninsula and the Tokat Massif (Anatolia), *Turk. J. Earth Sci.*, 19, 409–429, <https://doi.org/10.3906/yer-0910-39>, 2010.

Ferry, J. M. and Watson, E. B.: New thermodynamic models and revised calibrations for the Ti-in-zircon and Zr-in-rutile thermometers, *Contrib. Mineral. Petrol.*, 154, 429–437, <https://doi.org/10.1007/s00410-007-0201-0>, 2007.

640 Garzanti, E.: Petrographic classification of sand and sandstone, *Earth-Sci. Rev.*, <https://doi.org/10.1016/j.earscirev.2018.12.014>, 2018.

Garzanti, E. and Andò, S.: Heavy Mineral Concentration in Modern Sands: Implications for Provenance Interpretation, in: *Developments in Sedimentology*, vol. 58, edited by: Mange, M. A. and Wright, D. T., Elsevier, 517–545, [https://doi.org/10.1016/S0070-4571\(07\)58020-9](https://doi.org/10.1016/S0070-4571(07)58020-9), 2007.

645 Garzanti, E., Doglioni, C., Vezzoli, G., and Ando, S.: Orogenic belts and orogenic sediment provenance, *J. Geol.*, 115, 315–334, 2007.

Gaschnig, R. M.: Benefits of a Multiproxy Approach to Detrital Mineral Provenance Analysis: An Example from the Merrimack River, New England, USA, *Geochem. Geophys. Geosystems*, 20, 1557–1573, <https://doi.org/10.1029/2018GC008005>, 2019.

650 Gazzi, P.: On the Heavy Mineral Zones in the Geosyncline Series. Recent Studies in the Northern Apennines, Italy, *J. Sediment. Petrol.*, 35, 109–115, <https://doi.org/10.1306/74D71203-2B21-11D7-8648000102C1865D>, 1965.

Gehrels, G.: Detrital Zircon U-Pb Geochronology Applied to Tectonics, *Annu. Rev. Earth Planet. Sci.*, 42, 127–149, <https://doi.org/10.1146/annurev-earth-050212-124012>, 2014.

655 Göncüoğlu, M. C., Turhan, N., Şentürk, K., Özcan, A., Uysal, Ş., and Yaliniz, M. K.: A Geotraverse Across Northwestern Turkey: Tectonic Units of the Central Sakarya Region and their Tectonic Evolution, *Geol. Soc. Lond. Spec. Publ.*, 173, 139–161, <https://doi.org/10.1144/GSL.SP.2000.173.01.06>, 2000.

Guillong, M., Hametner, K., Reusser, E., Wilson, S. A., and Günther, D.: Preliminary Characterisation of New Glass Reference Materials (GSA-1G, GSC-1G, GSD-1G and GSE-1G) by Laser Ablation-Inductively Coupled Plasma-Mass Spectrometry



Using 193 nm, 213 nm and 266 nm Wavelengths, *Geostand. Geoanalytical Res.*, 29, 315–331, <https://doi.org/10.1111/j.1751-908X.2005.tb00903.x>, 2005.

Guo, R., Hu, X., Garzanti, E., Lai, W., Yan, B., and Mark, C.: How faithfully do the geochronological and geochemical signatures of detrital zircon, titanite, rutile and monazite record magmatic and metamorphic events? A case study from the Himalaya and Tibet, *Earth-Sci. Rev.*, 201, 103082, <https://doi.org/10.1016/j.earscirev.2020.103082>, 2020.

Hietpas, J., Samson, S., Moecher, D., and Schmitt, A. K.: Recovering tectonic events from the sedimentary record: Detrital monazite plays in high fidelity, *Geology*, 38, 167–170, <https://doi.org/10.1130/G30265.1>, 2010.

Hietpas, J., Samson, S., Moecher, D., and Chakraborty, S.: Enhancing tectonic and provenance information from detrital zircon studies: assessing terrane-scale sampling and grain-scale characterization, *J. Geol. Soc.*, 168, 309–318, <https://doi.org/10.1144/0016-76492009-163>, 2011.

Hubert, J. F.: Analysis of heavy-mineral assemblages, in: *Procedures in sedimentary petrology*, edited by: Carver, R. E., New York: Wiley-Interscience, 453–478, 1971.

Jochum, K. P., Willbold, M., Raczek, I., Stoll, B., and Herwig, K.: Chemical Characterisation of the USGS Reference Glasses GSA-1G, GSC-1G, GSD-1G, GSE-1G, BCR-2G, BHVO-2G and BIR-1G Using EPMA, ID-TIMS, ID-ICP-MS and LA-ICP-MS, *Geostand. Geoanalytical Res.*, 29, 285–302, <https://doi.org/10.1111/j.1751-908X.2005.tb00901.x>, 2005.

Jochum, K. P., Wilson, S. A., Abouchami, W., Amini, M., Chmeleff, J., Eisenhauer, A., Hegner, E., Iaccheri, L. M., Kieffer, B., Krause, J., McDonough, W. F., Mertz-Kraus, R., Raczek, I., Rudnick, R. L., Scholz, D., Steinhofel, G., Stoll, B., Stracke, A., Tonarini, S., Weis, D., Weis, U., and Woodhead, J. D.: GSD-1G and MPI-DING Reference Glasses for In Situ and Bulk Isotopic Determination, *Geostand. Geoanalytical Res.*, 35, 193–226, <https://doi.org/10.1111/j.1751-908X.2010.00114.x>, 2011.

Kasapoğlu, B., Ersoy, Y. E., Uysal, İ., Palmer, M. R., Zack, T., Koralay, E. O., and Karlsson, A.: The petrology of Paleogene volcanism in the Central Sakarya, Nallıhan Region: Implications for the initiation and evolution of post-collisional, slab break-off-related magmatic activity, *Lithos*, 246–247, 81–98, <https://doi.org/10.1016/j.lithos.2015.12.024>, 2016.

Kellett, D. A., Weller, O. M., Zagorevski, A., and Regis, D.: A petrochronological approach for the detrital record: Tracking mm-sized eclogite clasts in the northern Canadian Cordillera, *Earth Planet. Sci. Lett.*, 494, 23–31, <https://doi.org/10.1016/j.epsl.2018.04.036>, 2018.

Keskin, M. and Tüysüz, O.: Stratigraphy, petrogenesis and geodynamic setting of Late Cretaceous volcanism on the SW margin of the Black Sea, Turkey, *Geol. Soc. Lond. Spec. Publ.*, 464, 95–130, <https://doi.org/10.1144/SP464.5>, 2018.

Kohn, M. J.: A refined zirconium-in-rutile thermometer, *Am. Mineral.*, 105, 963–971, <https://doi.org/10.2138/am-2020-7091>, 2020.

Kohn, M. J. and Kelly, N. M.: Petrology and Geochronology of Metamorphic Zircon, in: *Geophysical Monograph Series*, edited by: Moser, D. E., Corfu, F., Darling, J. R., Reddy, S. M., and Tait, K., John Wiley & Sons, Inc., Hoboken, NJ, USA, 35–61, <https://doi.org/10.1002/9781119227250.ch2>, 2017.

Kooijman, E., Mezger, K., and Berndt, J.: Constraints on the U–Pb systematics of metamorphic rutile from in situ LA-ICP-MS analysis, *Earth Planet. Sci. Lett.*, 293, 321–330, <https://doi.org/10.1016/j.epsl.2010.02.047>, 2010.

Kooijman, E., Smit, M. A., Mezger, K., and Berndt, J.: Trace element systematics in granulite facies rutile: implications for Zr geothermometry and provenance studies, *J. Metamorph. Geol.*, 30, 397–412, <https://doi.org/10.1111/j.1525-1314.2012.00972.x>, 2012.



Kylander-Clark, A. R. C.: Slow subduction and exhumation of a thick ultrahigh -pressure terrane: Western Gneiss Region, Norway, Ph.D., University of California, Santa Barbara, United States -- California, 121 pp., 2008.

Lippert, P. G.: Detrital U-Pb geochronology provenance analyses: case studies in the Greater Green River Basin, Wyoming, and the Book Cliffs, Utah, Thesis, University of Kansas, 2014.

700 Ludwig, K. R.: On the Treatment of Concordant Uranium-Lead Ages, *Geochim. Cosmochim. Acta*, 62, 665–676, [https://doi.org/10.1016/S0016-7037\(98\)00059-3](https://doi.org/10.1016/S0016-7037(98)00059-3), 1998.

Luvizotto, G. L. and Zack, T.: Nb and Zr behavior in rutile during high-grade metamorphism and retrogression: An example from the Ivrea–Verbanò Zone, *Chem. Geol.*, 261, 303–317, <https://doi.org/10.1016/j.chemgeo.2008.07.023>, 2009.

705 Luvizotto, G. L., Zack, T., Meyer, H. P., Ludwig, T., Triebold, S., Kronz, A., Münker, C., Stockli, D. F., Prowatke, S., Klemme, S., Jacob, D. E., and von Eynatten, H.: Rutile crystals as potential trace element and isotope mineral standards for microanalysis, *Chem. Geol.*, 261, 346–369, <https://doi.org/10.1016/j.chemgeo.2008.04.012>, 2009.

Mange, M. A. and Maurer, H. F. W.: *Heavy Minerals in Colour*, Springer Dordrecht, 147 pp., 1992.

McLean, N. M., Bowring, J. F., and Bowring, S. A.: An algorithm for U-Pb isotope dilution data reduction and uncertainty propagation, *Geochem. Geophys. Geosystems*, 12, <https://doi.org/10.1029/2010GC003478>, 2011.

710 Meinhold, G.: Rutile and its applications in earth sciences, *Earth-Sci. Rev.*, 102, 1–28, <https://doi.org/10.1016/j.earscirev.2010.06.001>, 2010.

Meinhold, G., Anders, B., Kostopoulos, D., and Reischmann, T.: Rutile chemistry and thermometry as provenance indicator: An example from Chios Island, Greece, *Sediment. Geol.*, 203, 98–111, <https://doi.org/10.1016/j.sedgeo.2007.11.004>, 2008.

715 Moecher, D., Hietpas, J., Samson, S., and Chakraborty, S.: Insights into southern Appalachian tectonics from ages of detrital monazite and zircon in modern alluvium, *Geosphere*, 7, 494–512, <https://doi.org/10.1130/GES00615.1>, 2011.

Morton, A. C.: Heavy minerals in provenance studies, in: *Provenance of Arenites*, edited by: Zuffa, G. G., Reidel, Dordrecht, 249–277, 1985.

Morton, A. C. and Hallsworth, C.: Identifying provenance-specific features of detrital heavy mineral assemblages in sandstones, *Sediment. Geol.*, 90, 241–256, [https://doi.org/10.1016/0037-0738\(94\)90041-8](https://doi.org/10.1016/0037-0738(94)90041-8), 1994.

720 Mueller, M., Licht, A., Möller, A., Condit, C., Fosdick, J. C., Ocakoğlu, F., and Campbell, C.: Supplemental data for: An expanded workflow for detrital rutile provenance studies: An application from the Neotethys Orogen in Anatolia, <https://doi.org/10.17605/OSF.IO/A4YE5>, 2023.

725 Mueller, M. A., Licht, A., Campbell, C., Ocakoğlu, F., Taylor, M. H., Burch, L., Ugrai, T., Kaya, M., Kurtoğlu, B., Coster, P. M. C., Métais, G., and Beard, K. C.: Collision Chronology Along the İzmir-Ankara-Erzincan Suture Zone: Insights From the Sarıcakaya Basin, Western Anatolia, *Tectonics*, 38, 3652–3674, <https://doi.org/10.1029/2019TC005683>, 2019.

Mueller, M. A., Licht, A., Campbell, C., Ocakoğlu, F., Akşit, G. G., Métais, G., Coster, P. M. C., Beard, K. C., and Taylor, M. H.: Sedimentary Provenance From the Evolving Forearc-to-Foreland Central Sakarya Basin, Western Anatolia Reveals Multi-Phase Intercontinental Collision, *Geochem. Geophys. Geosystems*, 23, e2021GC010232, <https://doi.org/10.1029/2021GC010232>, 2022.





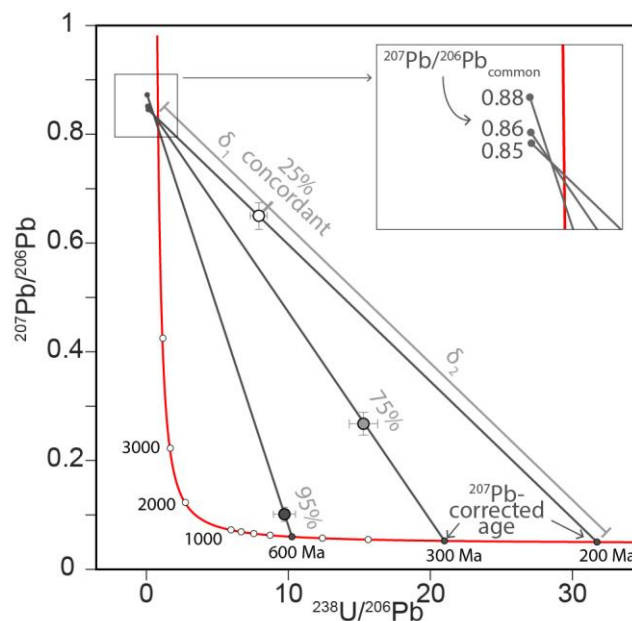
- 730 Nasdala, L., Pidgeon, R. T., Wolf, D., and Irmer, G.: Metamictization and U-PB isotopic discordance in single zircons: a combined Raman microprobe and SHRIMP ion probe study, *Mineral. Petrol.*, 62, 1–27, <https://doi.org/10.1007/BF01173760>, 1998.
- Ocakoğlu, F., Hakyemez, A., Açıkalin, S., Özkan Altın, S., Büyükmeriç, Y., Licht, A., Demircan, H., Şafak, Ü., Yıldız, A., Yılmaz, İ. Ö., Wagreich, M., and Campbell, C.: Chronology of subduction and collision along the İzmir-Ankara suture in Western Anatolia: records from the Central Sakarya Basin, *Int. Geol. Rev.*, 1–26, <https://doi.org/10.1080/00206814.2018.1507009>, 2018.
- Odlum, M. L., Stockli, D. F., Capaldi, T. N., Thomson, K. D., Clark, J., Puigdefàbregas, C., and Fildani, A.: Tectonic and sediment provenance evolution of the South Eastern Pyrenean foreland basins during rift margin inversion and orogenic uplift, *Tectonophysics*, 765, 226–248, <https://doi.org/10.1016/j.tecto.2019.05.008>, 2019.
- 740 Okay, A. I. and Göncüoğlu, M. C.: The Karakaya Complex: A Review of Data and Concepts, *Turk. J. Earth Sci.*, 13, 77–95, 2004.
- Okay, A. I. and Kylander-Clark, A. R. C.: No sediment transport across the Tethys ocean during the latest Cretaceous: detrital zircon record from the Pontides and the Anatolide–Tauride Block, *Int. J. Earth Sci.*, <https://doi.org/10.1007/s00531-022-02275-1>, 2022.
- 745 Okay, A. I., Monod, O., and Monié, P.: Triassic blueschists and eclogites from northwest Turkey: vestiges of the Paleo-Tethyan subduction, *Lithos*, 64, 155–178, [https://doi.org/10.1016/S0024-4937\(02\)00200-1](https://doi.org/10.1016/S0024-4937(02)00200-1), 2002.
- Okay, A. I., Sunal, G., Sherlock, S., Kylander-Clark, A. R. C., and Özcan, E.: İzmir-Ankara Suture as a Triassic to Cretaceous Plate Boundary—Data From Central Anatolia, *Tectonics*, 39, e2019TC005849, <https://doi.org/10.1029/2019TC005849>, 2020.
- Okay, N., Zack, T., Okay, A. I., and Barth, M.: Sinistral transport along the Trans-European Suture Zone: detrital zircon–rutile geochronology and sandstone petrography from the Carboniferous flysch of the Pontides, *Geol. Mag.*, 148, 380–403, <https://doi.org/10.1017/S0016756810000804>, 2011.
- Paterson, S. R. and Ducea, M. N.: Arc Magmatic Tempos: Gathering the Evidence, *Elements*, 11, 91–98, <https://doi.org/10.2113/gselements.11.2.91>, 2015.
- 755 Paton, C., Hellstrom, J., Paul, B., Woodhead, J., and Hergt, J.: Iolite: Freeware for the visualisation and processing of mass spectrometric data, *J. Anal. At. Spectrom.*, 26, 2508, <https://doi.org/10.1039/c1ja10172b>, 2011.
- Pereira, I. and Storey, C. D.: Detrital rutile: Records of the deep crust, ores and fluids, *Lithos*, 107010, <https://doi.org/10.1016/j.lithos.2022.107010>, 2023.
- Pereira, I., Storey, C. D., Strachan, R. A., Bento dos Santos, T., and Darling, J. R.: Detrital rutile ages can deduce the tectonic setting of sedimentary basins, *Earth Planet. Sci. Lett.*, 537, 116193, <https://doi.org/10.1016/j.epsl.2020.116193>, 2020.
- 760 Pickett, E. A. and Robertson, A. H. F.: Formation of the Late Palaeozoic–Early Mesozoic Karakaya Complex and related ophiolites in NW Turkey by Palaeotethyan subduction–accretion, *J. Geol. Soc.*, 153, 995–1009, <https://doi.org/10.1144/gsjgs.153.6.0995>, 1996.
- Rösel, D., Boger, S. D., Möller, A., Gaitzsch, B., Barth, M., Oalmann, J., and Zack, T.: Indo-Antarctic derived detritus on the northern margin of Gondwana: evidence for continental-scale sediment transport, *Terra Nova*, 26, 64–71, <https://doi.org/10.1111/ter.12070>, 2014.
- 765



- Rösel, D., Zack, T., and Möller, A.: Interpretation and significance of combined trace element and U–Pb isotopic data of detrital rutile: a case study from late Ordovician sedimentary rocks of Saxo-Thuringia, Germany, *Int. J. Earth Sci.*, 108, 1–25, <https://doi.org/10.1007/s00531-018-1643-5>, 2019.
- 770 Rosenblum, S. and Brownfield, I. K.: Magnetic susceptibilities of minerals, *Magnetic susceptibilities of minerals*, U.S. Geological Survey, Reston, VA, <https://doi.org/10.3133/ofr99529>, 2000.
- Rudnick, R., Barth, M., Horn, I., and McDonough, W. F.: Rutile-Bearing Refractory Eclogites: Missing Link Between Continents and Depleted Mantle, *Science*, 287, 278–281, <https://doi.org/10.1126/science.287.5451.278>, 2000.
- Schoene, B.: U–Th–Pb Geochronology, in: *Treatise on Geochemistry*, Elsevier, 341–378, <https://doi.org/10.1016/B978-0-08-095975-7.00310-7>, 2014.
- 775 Schwarz, D.: *Fast and Robust Curve Intersections*, 2022.
- Şengör, A. M. C. and Yilmaz, Y.: Tethyan evolution of turkey: a plate tectonic approach, *Tectonophysics*, 75, 181–241, 1981.
- Şengün, F., Zack, T., and Dunkl, I.: Provenance of detrital rutiles from the Jurassic sandstones in the Central Sakarya Zone, NW Turkey: U–Pb ages and trace element geochemistry, *Geochemistry*, 80, 125667, <https://doi.org/10.1016/j.chemer.2020.125667>, 2020.
- 780 Sharman, G. R., Sharman, J. P., and Sylvester, Z.: detritalPy: A Python-based toolset for visualizing and analysing detrital geo-thermochronologic data, *Depositional Rec.*, 4, 202–215, <https://doi.org/10.1002/dep2.45>, 2018.
- Shekut, S. and Licht, A.: Late Middle Miocene Emergence of the Olympic Peninsula Shown by Sedimentary Provenance, *Lithosphere*, 2020, 1–20, <https://doi.org/10.2113/2020/7040598>, 2020.
- 785 Stacey, J. S. and Kramers, J. D.: Approximation of terrestrial lead isotope evolution by a two-stage model, *Earth Planet. Sci. Lett.*, 26, 207–221, [https://doi.org/10.1016/0012-821X\(75\)90088-6](https://doi.org/10.1016/0012-821X(75)90088-6), 1975.
- Sundell, K. E., George, S. W. M., Carrapa, B., Gehrels, G. E., Ducea, M. N., Saylor, J. E., and Pepper, M.: Crustal Thickening of the Northern Central Andean Plateau Inferred From Trace Elements in Zircon, *Geophys. Res. Lett.*, 49, e2021GL096443, <https://doi.org/10.1029/2021GL096443>, 2022.
- 790 Tang, M., Ji, W.-Q., Chu, X., Wu, A., and Chen, C.: Reconstructing crustal thickness evolution from europium anomalies in detrital zircons, *Geology*, 49, 76–80, <https://doi.org/10.1130/G47745.1>, 2020.
- Tera, F. and Wasserburg, G. J.: U–Th–Pb systematics in three Apollo 14 basalts and the problem of initial Pb in lunar rocks, *Earth Planet. Sci. Lett.*, 14, 281–304, [https://doi.org/10.1016/0012-821X\(72\)90128-8](https://doi.org/10.1016/0012-821X(72)90128-8), 1972.
- The MathWorks Inc.: MATLAB Version: 9.11.0.1873467 (R2021b) Update 3, 2021.
- 795 Tomkins, H. S., Powell, R., and Ellis, D. J.: The pressure dependence of the zirconium-in-rutile thermometer, *J. Metamorph. Geol.*, 25, 703–713, <https://doi.org/10.1111/j.1525-1314.2007.00724.x>, 2007.
- Topuz, G., Candan, O., Okay, A. I., von Quadt, A., Othman, M., Zack, T., and Wang, J.: Silurian anorogenic basic and acidic magmatism in Northwest Turkey: Implications for the opening of the Paleo-Tethys, *Lithos*, 356–357, 105302, <https://doi.org/10.1016/j.lithos.2019.105302>, 2020.



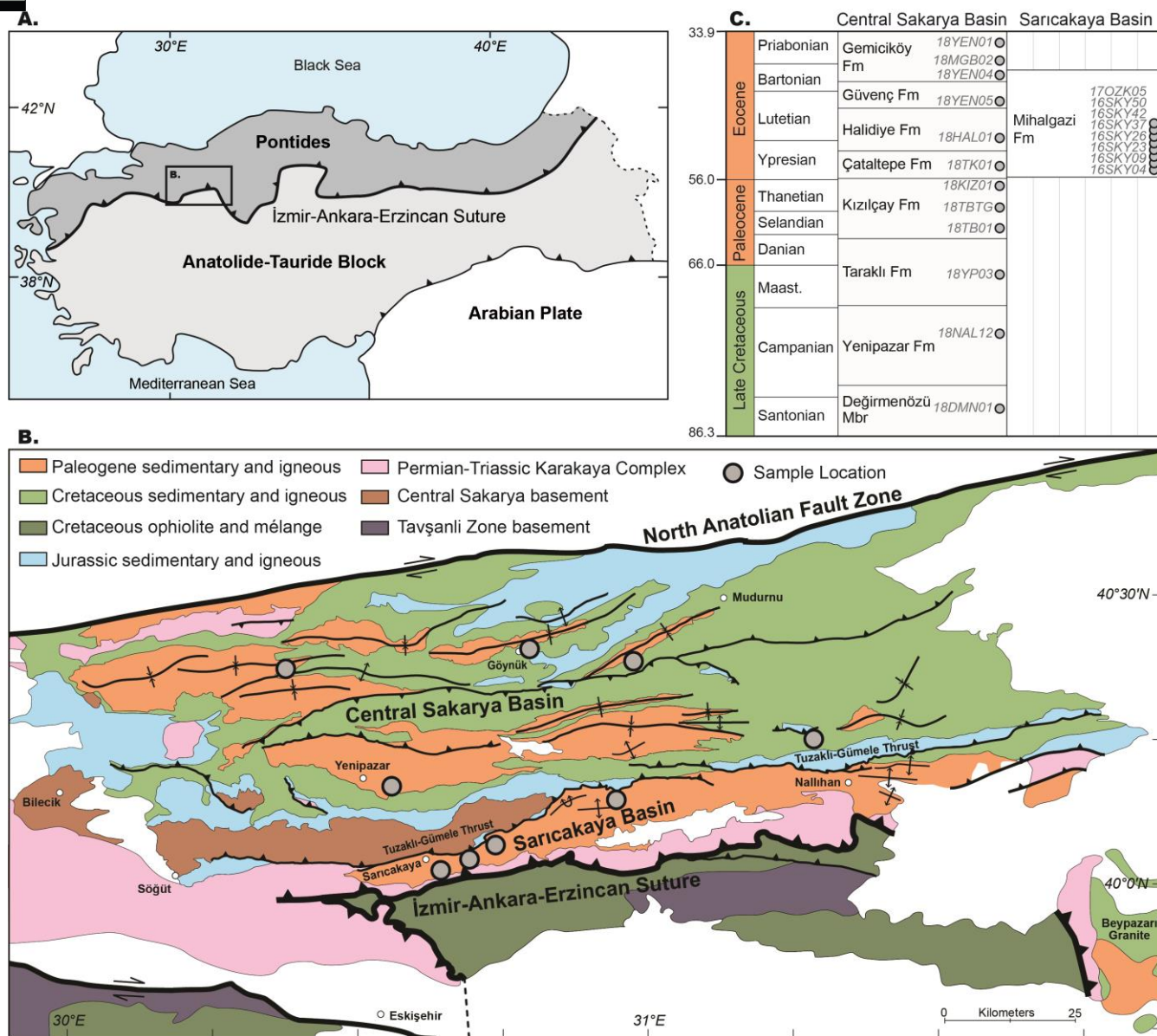
- Triebold, S., von Eynatten, H., Luvizotto, G. L., and Zack, T.: Deducing source rock lithology from detrital rutile geochemistry: An example from the Erzgebirge, Germany, *Chem. Geol.*, 244, 421–436, <https://doi.org/10.1016/j.chemgeo.2007.06.033>, 2007.
- Triebold, S., Luvizotto, G. L., Tolosana-Delgado, R., Zack, T., and von Eynatten, H.: Discrimination of TiO<sub>2</sub> polymorphs in sedimentary and metamorphic rocks, *Contrib. Mineral. Petrol.*, 161, 581–596, <https://doi.org/10.1007/s00410-010-0551-x>, 2011.
- 805 Triebold, S., von Eynatten, H., and Zack, T.: A recipe for the use of rutile in sedimentary provenance analysis, *Sediment. Geol.*, 282, 268–275, <https://doi.org/10.1016/j.sedgeo.2012.09.008>, 2012.
- Ustaömer, P., Ustaömer, T., and Robertson, Alastair. H. F.: Ion Probe U-Pb Dating of the Central Sakarya Basement: A peri-Gondwana Terrane Intruded by Late Lower Carboniferous Subduction/Collision-related Granitic Rocks, *Turk. J. Earth Sci.*, 21, 905–932, <https://doi.org/10.3906/yer-1103-1>, 2012.
- 810 Ustaömer, T., Ustaömer, P., Robertson, A. H. F., and Gerdes, A.: Implications of U–Pb and Lu–Hf isotopic analysis of detrital zircons for the depositional age, provenance and tectonic setting of the Permian–Triassic Palaeotethyan Karakaya Complex, NW Turkey, *Int. J. Earth Sci.*, 105, 7–38, <https://doi.org/10.1007/s00531-015-1225-8>, 2016.
- Vermeesch, P.: IsoplotR: A free and open toolbox for geochronology, *Geosci. Front.*, 9, 1479–1493, <https://doi.org/10.1016/j.gsf.2018.04.001>, 2018.
- 815 Vermeesch, P.: Unifying the U–Pb and Th–Pb methods: joint isochron regression and common Pb correction, *Geochronology*, 2, 119–131, <https://doi.org/10.5194/gchron-2-119-2020>, 2020.
- Vermeesch, P.: On the treatment of discordant detrital zircon U–Pb data, *Geochronology*, 3, 247–257, <https://doi.org/10.5194/gchron-3-247-2021>, 2021.
- Watson, E. B., Wark, D. A., and Thomas, J. B.: Crystallization thermometers for zircon and rutile, *Contrib. Mineral. Petrol.*, 820 151, 413, <https://doi.org/10.1007/s00410-006-0068-5>, 2006.
- Zack, T. and Kooijman, E.: Petrochronology and Geochronology of Rutile, *Rev. Mineral. Geochem.*, 83, 443–467, 2017.
- Zack, T., von Eynatten, H., and Kronz, A.: Rutile geochemistry and its potential use in quantitative provenance studies, *Sediment. Geol.*, 171, 37–58, <https://doi.org/10.1016/j.sedgeo.2004.05.009>, 2004a.
- 825 Zack, T., Moraes, R., and Kronz, A.: Temperature dependence of Zr in rutile: empirical calibration of a rutile thermometer, *Contrib. Mineral. Petrol.*, 148, 471–488, <https://doi.org/10.1007/s00410-004-0617-8>, 2004b.
- Zack, T., Stockli, D. F., Luvizotto, G. L., Barth, M. G., Belousova, E., Wolfe, M. R., and Hinton, R. W.: In situ U–Pb rutile dating by LA-ICP-MS: 208Pb correction and prospects for geological applications, *Contrib. Mineral. Petrol.*, 162, 515–530, <https://doi.org/10.1007/s00410-011-0609-4>, 2011.



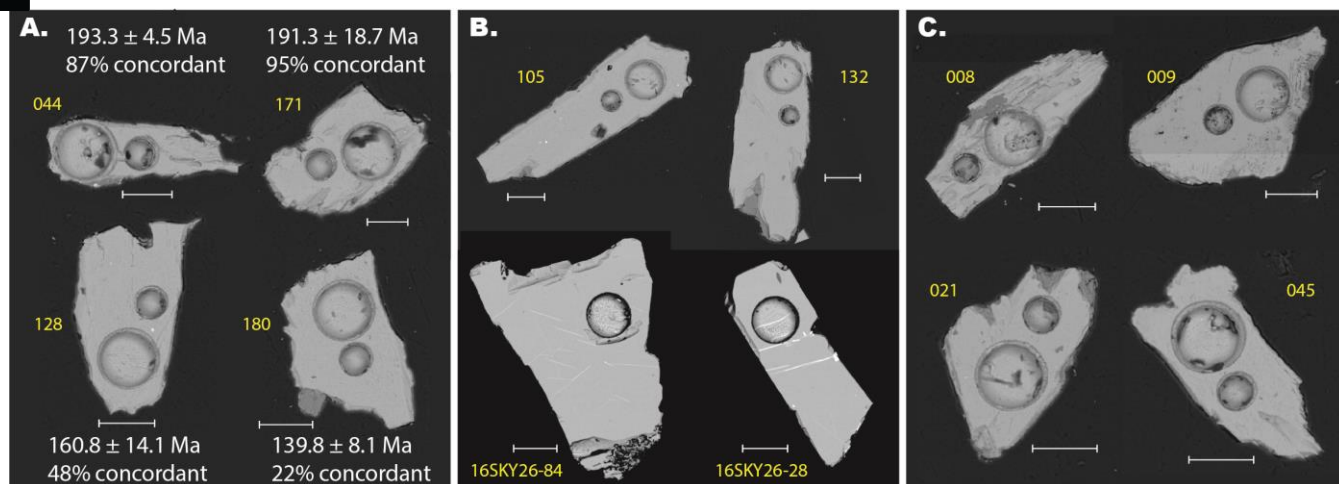
830

**Figure 1: Conceptual schematic of the  $^{207}\text{Pb}$  correction in Tera-Wasserburg space (after Vermeesch, 2021). First, the common  $^{207}\text{Pb}/^{206}\text{Pb}$  ratio is calculated from the initial date estimate (i.e.,  $t_1$  or  $t_{208}$ , see text for details). Next, a discordia is fitted between  $^{207}\text{Pb}/^{206}\text{Pb}_{\text{common}}$  and the data point. Then, the lower intersection of the line with the concordia marks the corrected  $^{238}\text{U}/^{206}\text{Pb}$  and  $^{207}\text{Pb}/^{206}\text{Pb}$ , which are used to calculate the  $^{207}\text{Pb}$ -corrected date. Concordance is defined as the distance along the discordia between the upper and lower intersections of the discordia with the concordia (Eqn. 7).**

835

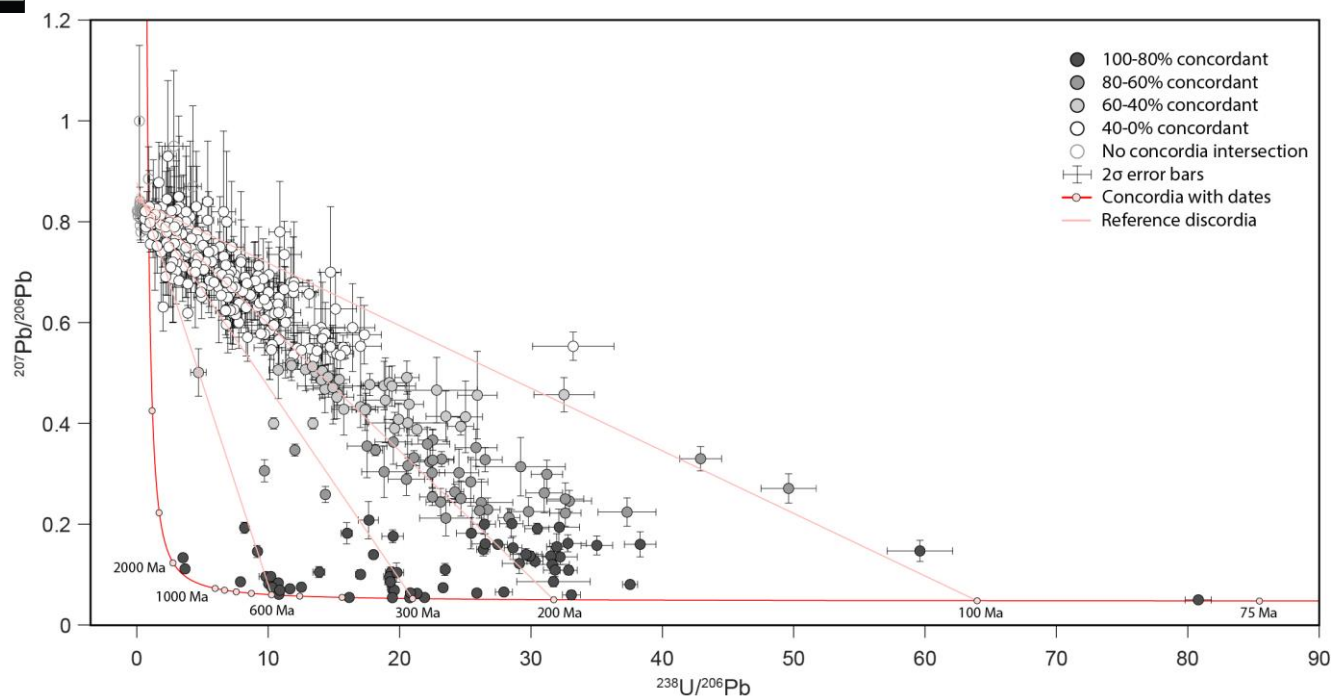


**Figure 2:** (A) Simplified terrane map of Anatolia and (B) geologic map of the Central Sakarya Basin and Sarıcakaya Basin region (after Aksay et al., 2002). (C) Simplified stratigraphic correlation chart and schematic sample distribution. Stratigraphy after Ocakoğlu et al. (2018).



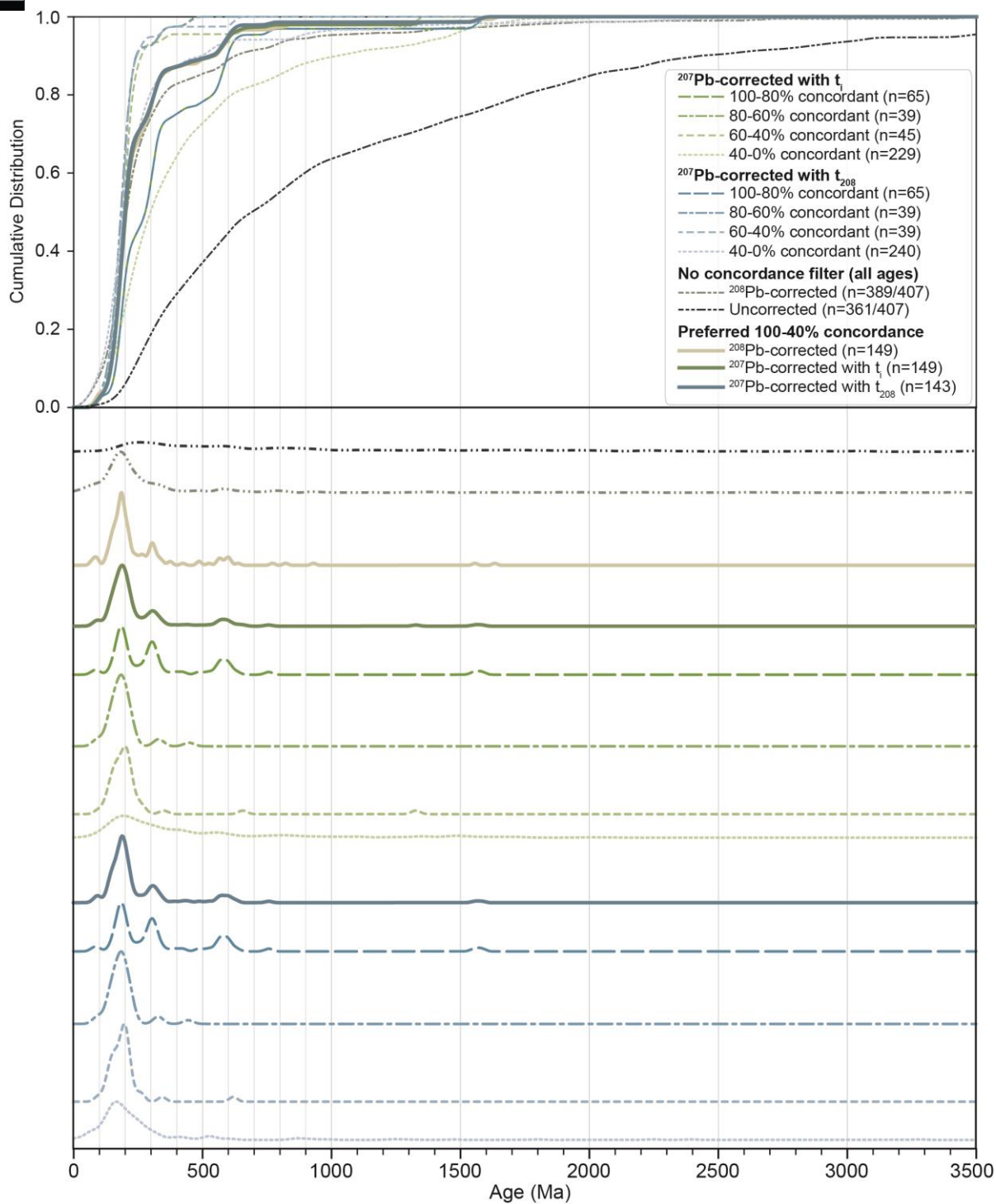
845 **Figure 3: SEM BSE images of representative rutile grains. All grains are from sample 18TK01 unless otherwise noted; the grain number is in yellow. Ablation pits are from U-Pb analysis (larger) and trace element analysis (smaller). (A) Rutile analyses with acceptable U-Pb dates across a range of concordance. U-Pb date and concordance is from  $^{207}\text{Pb}_{\text{Ti}}$  correction method. (B) Rutile analyses rejected because of inclusions (top) or exsolution lamellae (bottom). (C) Rutile analyses discarded for anomalous signal intensity (spiky signal). The scale bar is 50  $\mu\text{m}$ .**



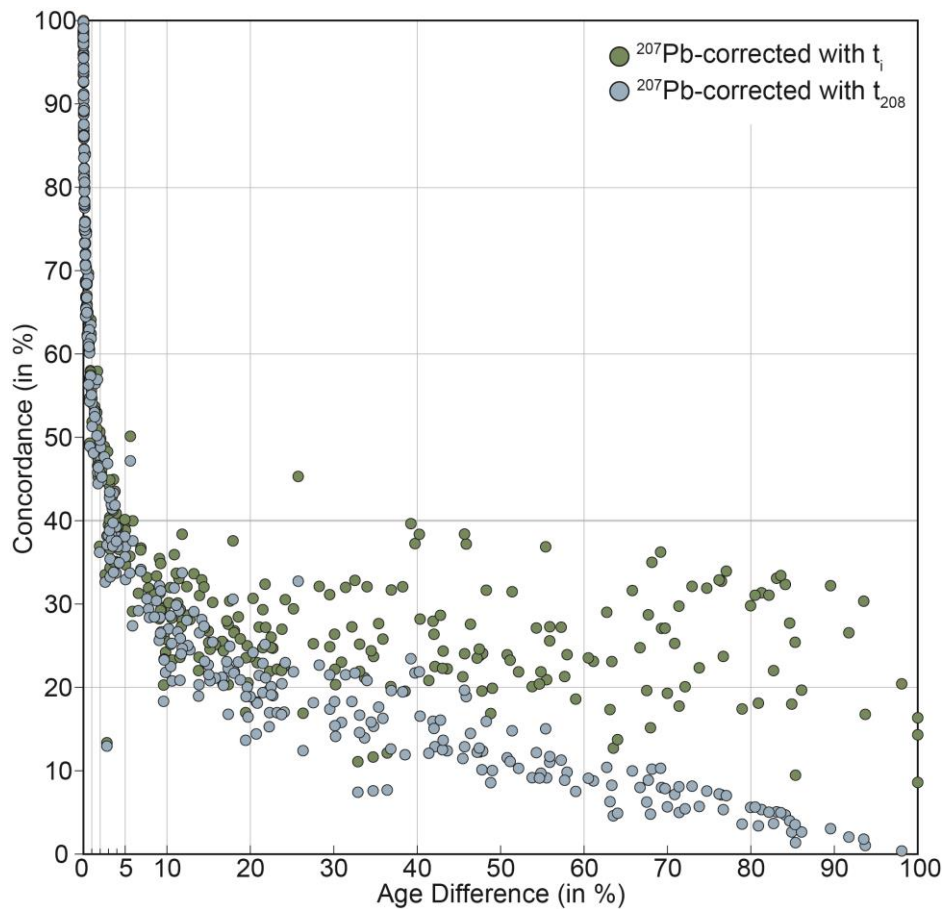


850 **Figure 4: Detrital rutile U-Pb results displayed in Tera-Wasserburg space. Data points are colored by discordance bins, error bars are 2σ. Shown for reference are discordia lines towards lower intercepts at 100, 200, 300, and 600 Ma (pink lines).**

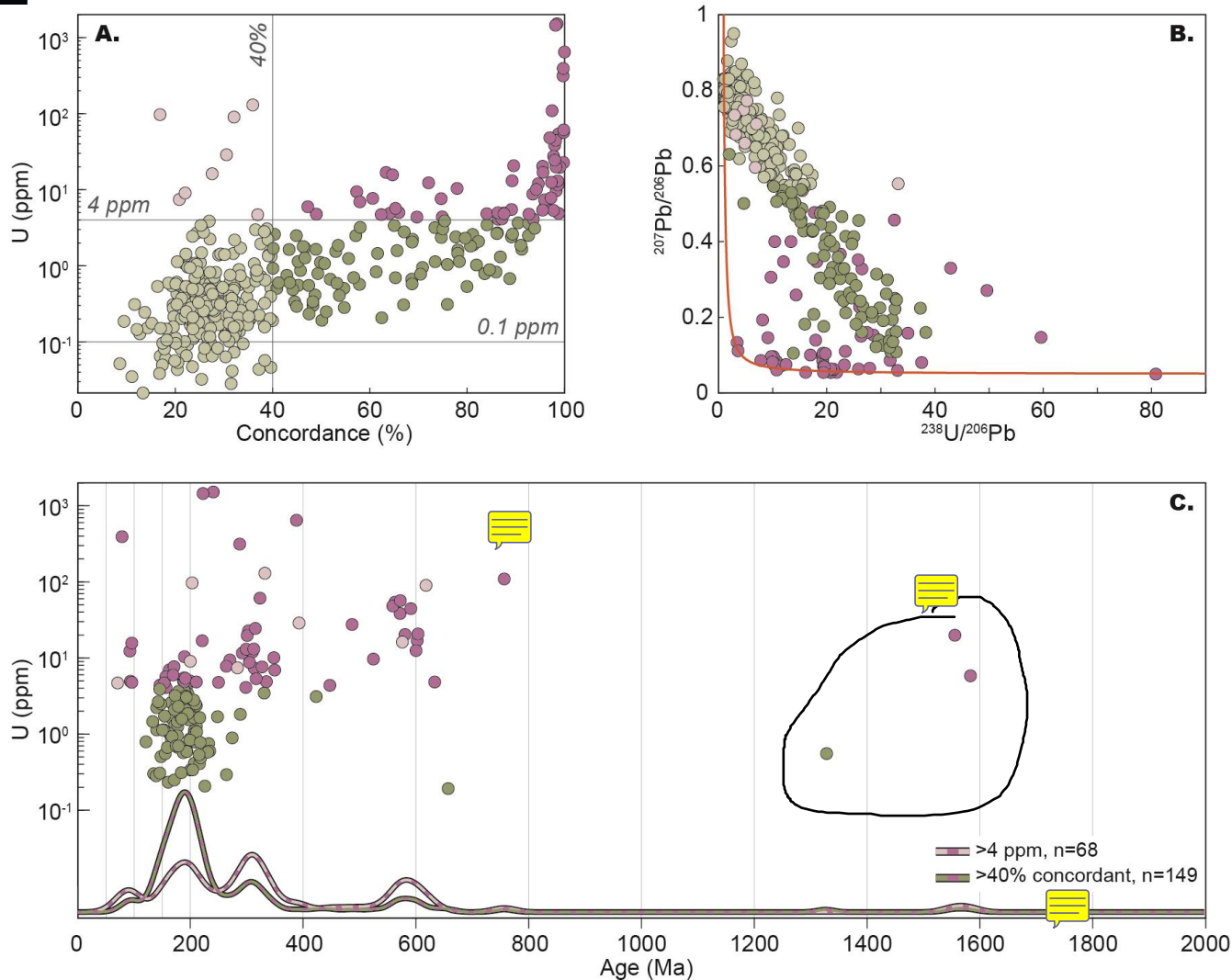




**Figure 5: Distributions of dates of all samples together shown as kernel density estimates (KDEs) and cumulative distribution functions visualized with detritalPy (Sharman et al., 2018). Uncorrected and corrected data are separated into concordance bins. Solid line KDEs represent the data with our preferred 100-40% concordance range.**



**Figure 6: Concordance versus the difference in  $^{207}\text{Pb}$ -corrected dates using  $t_1$  or  $t_{208}$ . The largest differences in age are for grains that are less than 40% concordant.**



860

Figure 7: Comparison of detrital rutile filtering based on U concentration or concordance. (A) Rutile U concentration versus percent concordance. U-threshold filtering includes all grains greater than 4 ppm (pink colors), whereas concordance-threshold filtering includes grains greater than 40% (dark pink and dark green colors). (B) Rutile U-Pb results in Tera-Wasserburg space following the color scheme in panel A. (C) Rutile U concentration versus  $^{207}\text{Pb}_{\text{Ti}}$ -corrected U-Pb date. The KDEs display the date spectra from the different filtering protocols. Rutile with less than 4 ppm and less than 40% concordance are excluded by both filters and not included in panel C.

865

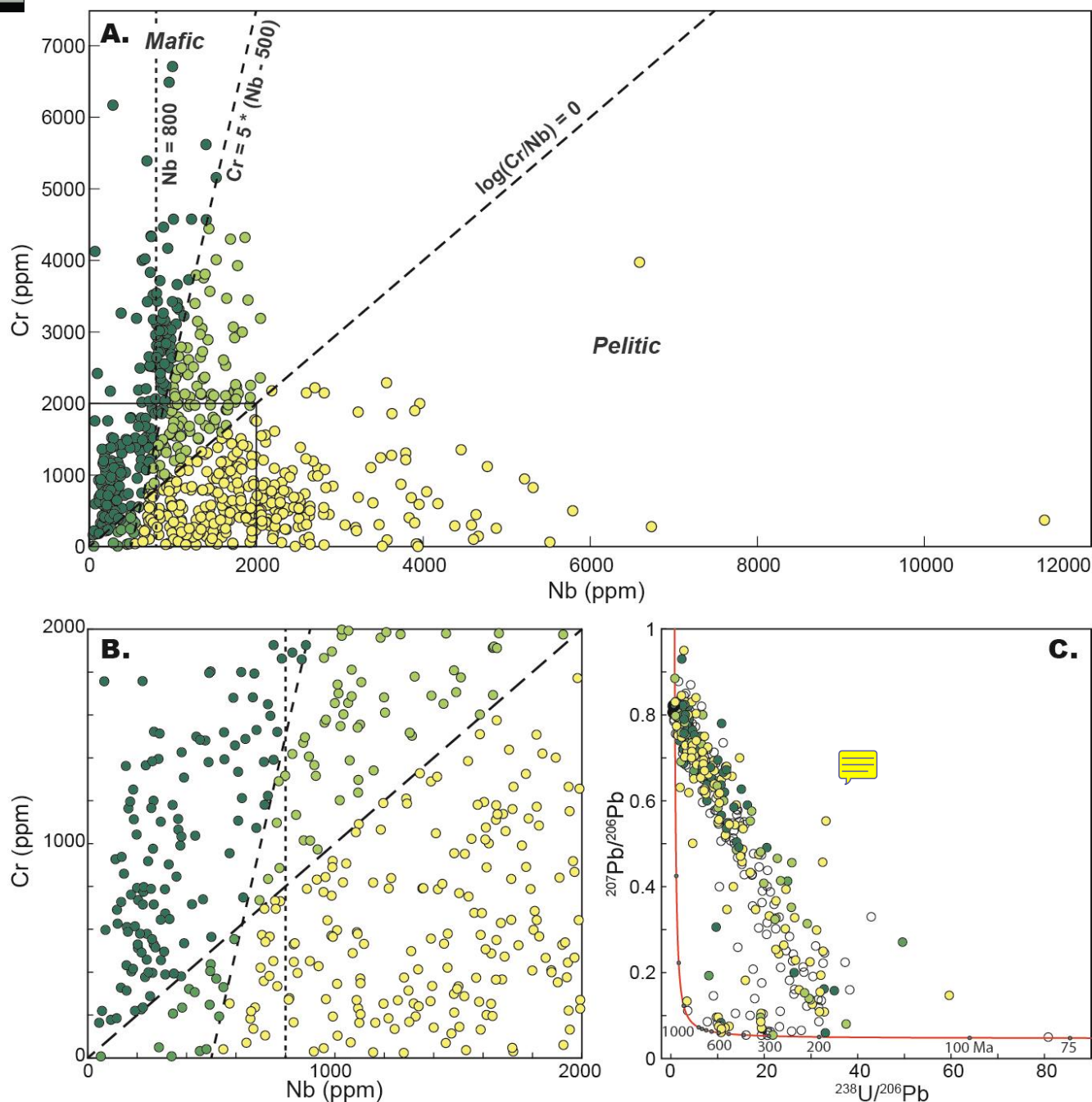
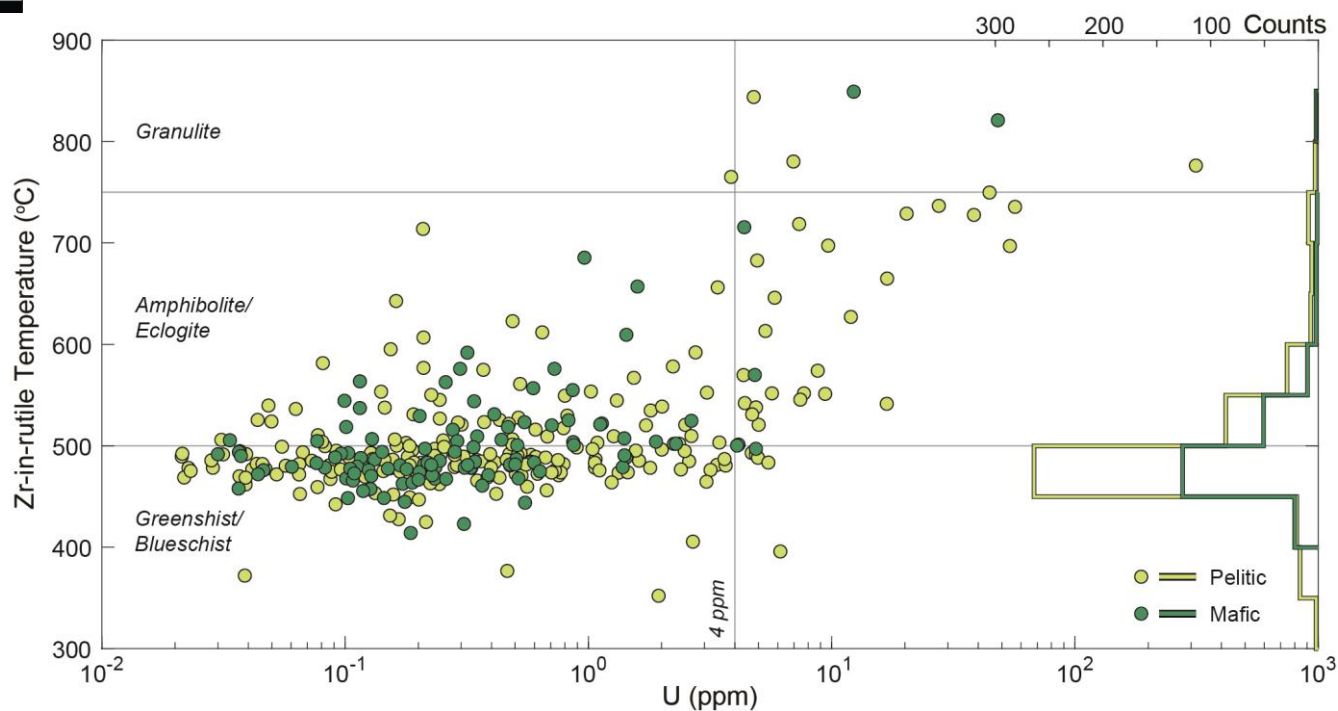

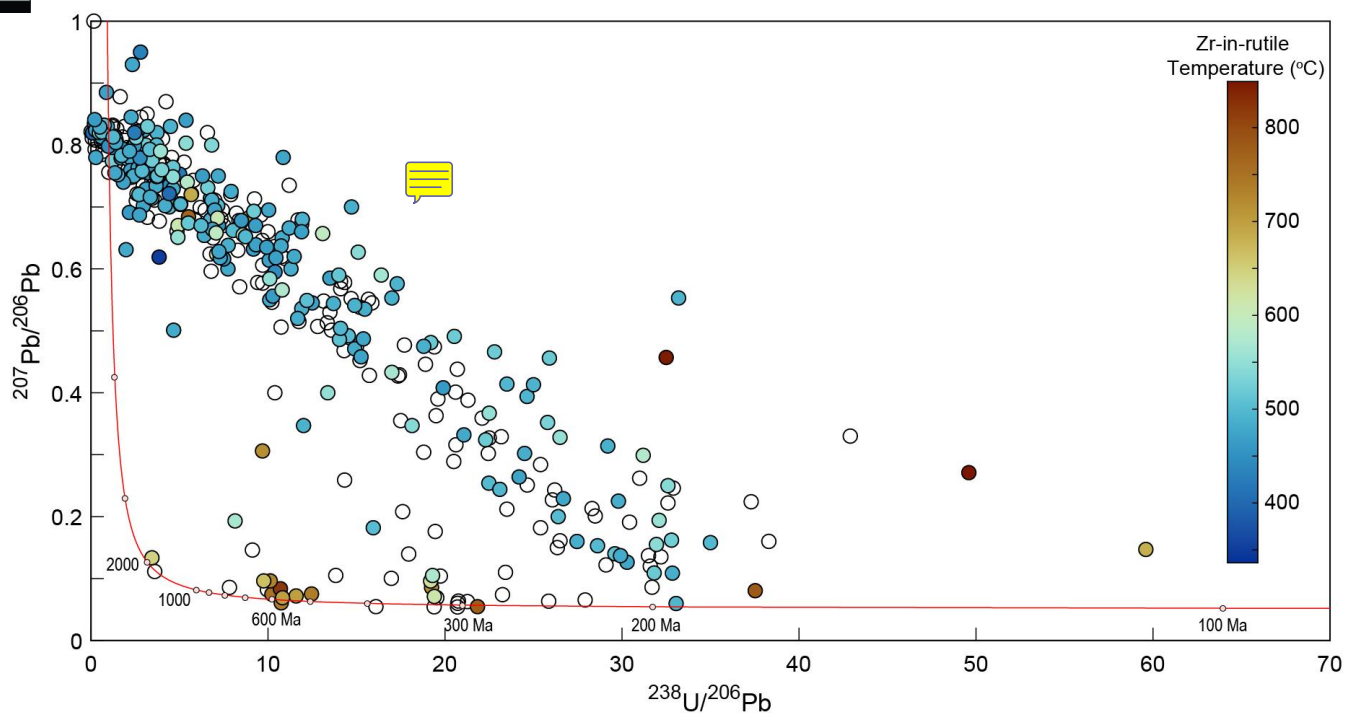


Figure 8: Cr versus Nb discrimination diagrams for detrital rutile from this study (A and B). Dashed lines demarcate proposed boundaries between mafic and pelitic source fields (Triebold et al., 2007, 2012; Meinhold et al., 2008). Rutile grains are colored by their respective source field. (C) Rutile analyses in Tera-Wasserburg space reveal mixed source lithologies in each date mode. Unfilled circles are rutile U-Pb analyses without trace element data.

870

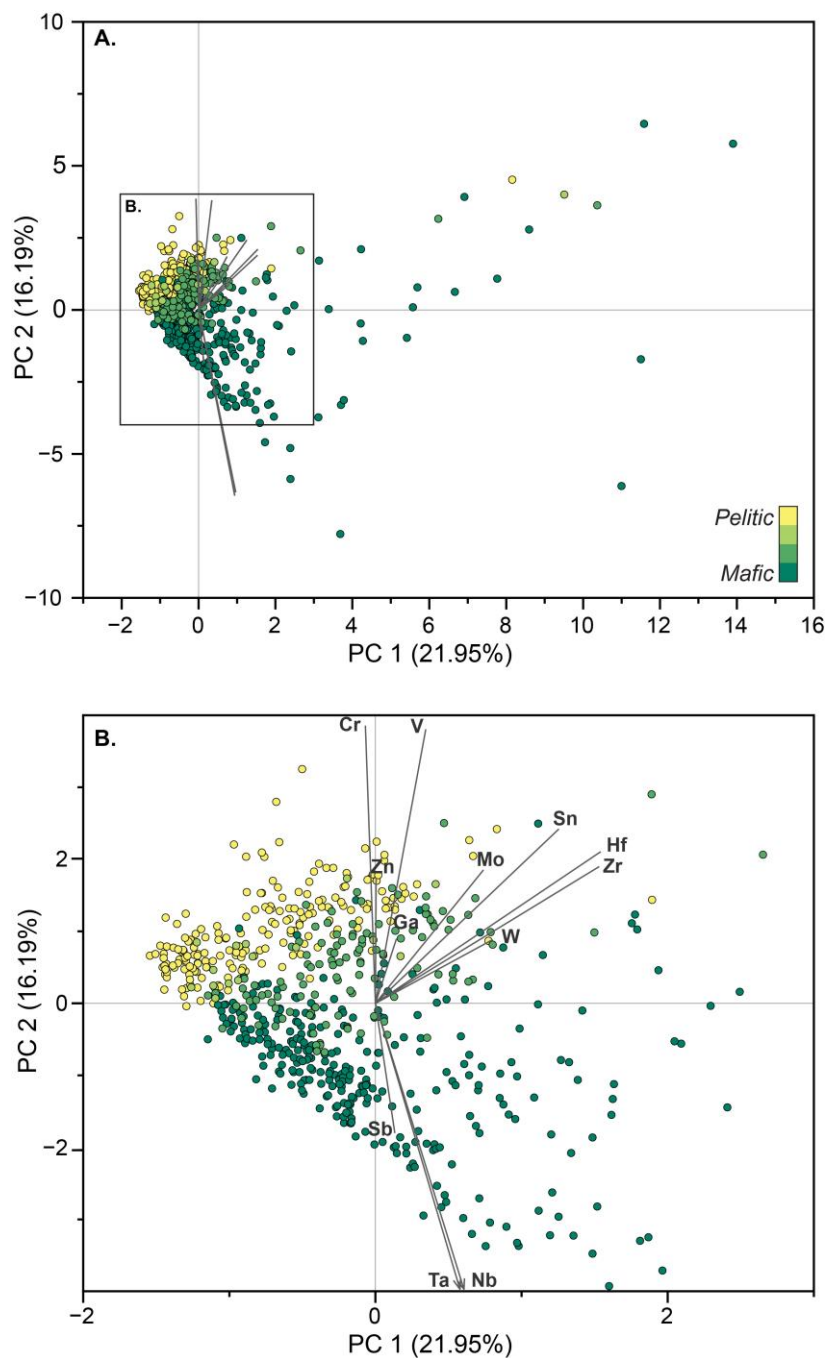


875 **Figure 9: Zr-in-rutile temperature versus U concentration. Mafic and pelitic scores are from the Triebold et al. (2012) discrimination (i.e.,  $Cr = 5 * [Nb - 500]$ ): mafic grains include the combined dark green colors from Figure 8 and pelitic include the light green and yellow colors. Zr-in-rutile temperatures follow the Kohn (2020) calibration.  histogram shows the distribution of mafic and pelitic grains by temperature. Note that not all analyses have both U and  $T_{Zr}$  data, therefore there are fewer grains represented in the scatter plot than in the histogram and Figure 8A.**



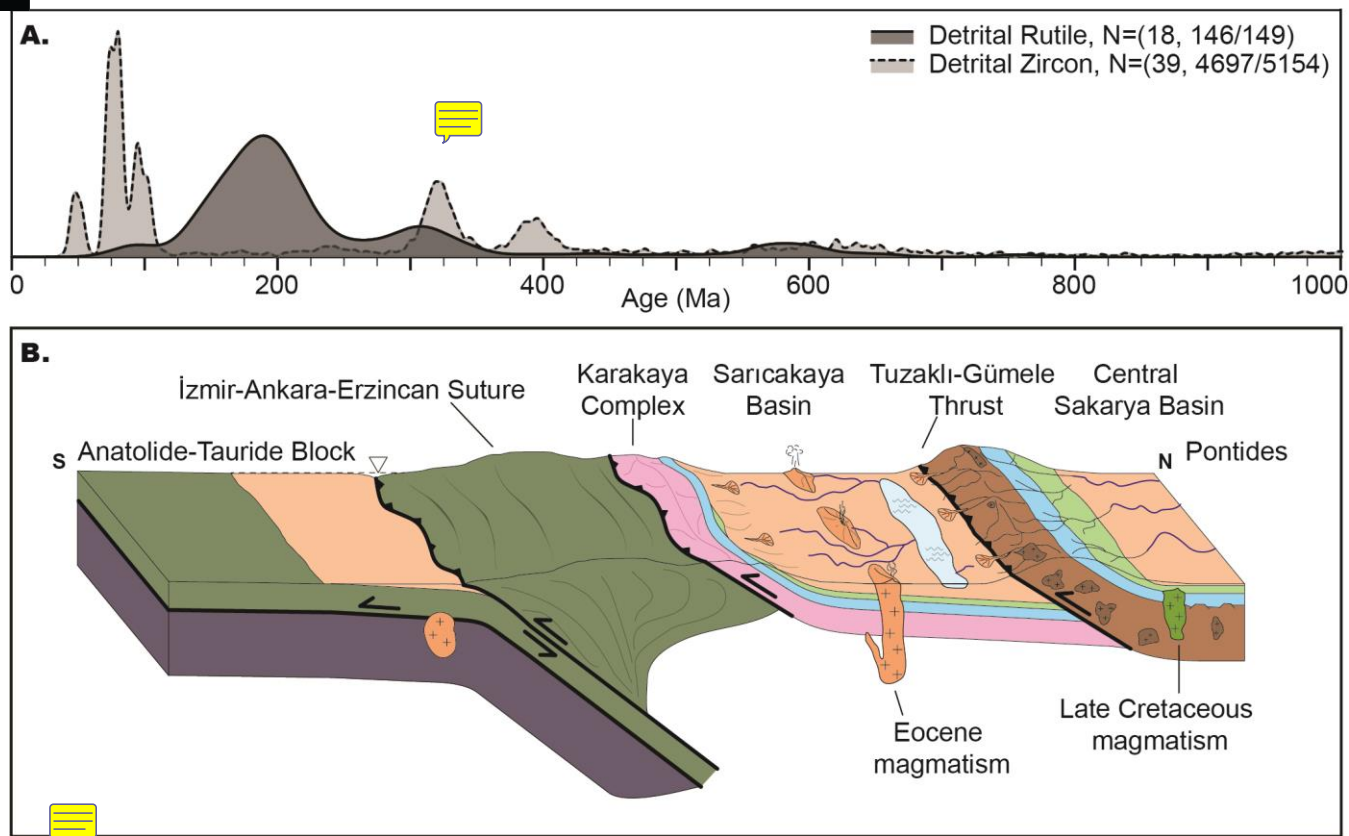
880 **Figure 10: Rutile U-Pb results in Tera-Wasserburg space colored by Zr-in-rutile temperature calculated from the Kohn (2020) calibration. The mode centered around 95 Ma has the highest temperatures, and modes centered around 310 Ma and 580 Ma also contain high temperatures, whereas the 190 Ma mode is predominantly composed of lower temperature grains. Unfilled circles are rutile U-Pb analyses without trace element data. Colormap is from Crameri (2020).**





885 **Figure 11: PCA score and loadings plot of principal components 1 and 2, which cumulatively explain 38.14% of trace element variance. Sample points are colored by mafic and pelitic scores from Cr/Nb discrimination shown in Figure 8. The variance in trace element chemistry is best explained by metamorphic grade (PC 1) and protolith (PC 2).**





890 **Figure 12.** (A) Kernel density estimate of all detrital rutile ages ( $^{207}\text{Pb}_{\text{ti}}$ -corrected) shown alongside a compilation of all published detrital zircon ages from Upper Cretaceous to Eocene strata in Central Sakarya and Sarıcakaya Basins. (B) Schematic reconstruction of northwestern Anatolia in the Eocene during continental collision (after Mueller et al., 2019). The main sources of sediment to the basins were the Karakaya Complex exposed in the suture zone, Pontides crystalline basement exposed along the Tuzaklı-Gümele Thrust, Cretaceous-Eocene igneous units, and recycled sedimentary units.